Computational Geosciences
https://doi.org/10.1007/s10596-018-9793-x

ORIGINAL PAPER

Benchmarking of reactive transport codes for 2D simulations with mineral dissolution–precipitation reactions and feedback on transport parameters

J. Poonoosamy[1,5] · C. Wanner[2] · P. Alt Epping[2] · J. F. Águila[3] · J. Samper[3] · L. Montenegro[3] · M. Xie[4] · D. Su[4] · K. U. Mayer[4] · U. Mäder[2] · L. R. Van Loon[1] · G. Kosakowski[1]

Received: 9 May 2018 / Accepted: 17 October 2018

Abstract

Porosity changes due to mineral dissolution–precipitation reactions in porous media and the resulting impact on transport parameters influence the evolution of natural geological environments or engineered underground barrier systems. In the absence of long-term experimental studies, reactive transport codes are used to evaluate the long-term evolution of engineered barrier systems and waste disposal in the deep underground. Examples for such problems are the long-term fate of CO_2 in saline aquifers and mineral transformations that cause porosity changes at clay–concrete interfaces. For porosity clogging under a diffusive transport regime and for simple reaction networks, the accuracy of numerical codes can be verified against analytical solutions. For clogging problems with more complex chemical interactions and transport processes, numerical benchmarks are more suitable to assess model performance, the influence of thermodynamic data, and sensitivity to the reacting mineral phases. Such studies increase confidence in numerical model descriptions of more complex, engineered barrier systems. We propose a reactive transport benchmark, considering the advective–diffusive transport of solutes; the effect of liquid-phase density on liquid flow and advective transport; kinetically controlled dissolution–precipitation reactions causing porosity, permeability, and diffusivity changes; and the formation of a solid solution. We present and analyze the results of five participating reactive transport codes (i.e., CORE^{2D}, MIN3P-THCm, OpenGeoSys-GEM, PFLOTRAN, and TOUGHREACT). In all cases, good agreement of the results was obtained.

Keywords Benchmarking · Density-driven flow · Solid solution · Clogging · Barium sulfate · Strontium sulfate

1 Introduction

Water–rock interactions are important processes that govern the evolution of many natural and anthropogenic systems in the underground. These interactions include mineral precipitation and dissolution, sorption, and redox reactions. Mineral precipitation and dissolution generally modify the pore space geometry of rocks, which, in turn, changes flow and influences transport properties. Porosity changes induced by chemical interactions may alter the behavior or performance of natural and engineered systems including treatment for contaminated groundwater, CO_2 storage in deep geological formations, and CO_2-enhanced oil recovery in carbonate reservoirs and also at clay–cement interfaces in high-level nuclear waste repositories.

The investigation of many natural and artificial geosystems, in which the coupling of chemical reactions and

Electronic supplementary material The online version of this article (https://doi.org/10.1007/s10596-018-9793-x) contains supplementary material, which is available to authorized users.

✉ J. Poonoosamy
j.poonoosamy@fz-juelich.de

[1] Laboratory for Waste Management, Paul Scherrer Institut (PSI), 5232 Villigen, Switzerland

[2] Rock Water Interaction, Institute of Geological Sciences, University of Bern, Baltzerstrasse 3, 3012 Bern, Switzerland

[3] Centro de Investigaciones Científicas Avanzadas (CICA), E.T.S. Ingenieros de Caminos, Canales y Puertos, Campus de Elviña, Universidade de A Coruña, 15071 A Coruña, Spain

[4] Department of Earth, Ocean and Atmospheric Sciences, University of British Colombia, 2020–2207 Main Mall, Vancouver, BC V6T 1Z4, Canada

[5] Present address: Forschungszentrum Jülich GmbH, IEK-6: Institute of Nuclear Waste Management and Reactor Safety, 52425 Jülich, Germany

Published online: 19 November 2018

transport is important, is often done by means of reactive transport models because information on their geochemical evolution in space and time is scarce. Reactive transport models are numerical codes that solve a coupled set of equations, which describe the transport of mobile chemical species together with a variety of geochemical reactions. However, the predictions of reactive transport codes are sensitive to the intrinsic coupling of transport and chemical solvers. Application fields of reactive transport models include geothermal systems [1–4], nuclear waste repositories [5–9], geological carbon dioxide storage [10–12], and environmental remediation [13–15].

There is a need to verify the implementation and to evaluate the capabilities and performance of reactive transport codes. This process is called "benchmarking" and is normally done by comparing model results with analytical solutions, by reproducing results from laboratory or field experiments, and by code intercomparison. Benchmarking with porosity enhancement, reduction, or clogging is of great interest because of their strong influence on the coupling between transport and chemistry, commonly encountered in real geosystems.

Finding the exact solution for simplified 1D and 2D systems is the most preferred method to verify the numerical implementation of reactive transport codes. Analytical solutions for problems coupled with porosity changes are few. The only investigations on this topic include Lagneau and van der Lee [16] and Hayek et al. [17, 18]. Lagneau and van der Lee [16] proposed an analytical solution for a 1D system containing one species and one mineral. The analytical solution was used to verify the implementation of porosity changes in the reactive transport code HYTEC [19]. Their solution was only applicable to small and moderate porosity changes. Hayek et al. [17] developed analytical solutions for a 1D coupled diffusion–reaction problem with feedback on porosity change for benchmarking reactive transport. Their numerical experiment consisted in the precipitation of a solid phase from two aqueous species inside a porous medium, leading to strong porosity reduction and even clogging. They proposed analytical solutions that were only suitable for non-equilibrium chemistry. The good agreement between numerical and analytical solutions was obtained when sufficient spatial and temporal discretization was used for the numerical solution. Their simulation also demonstrated that, in agreement with Lagneau and van der Lee [16], numerical codes with explicit schemes did not always converge to the analytical solution. Only implicit schemes produced accurate solutions independent of time stepping. Analytical solutions describing transport of several aqueous species coupled with precipitation and dissolution of a single mineral in two and three dimensions with porosity change were proposed by Hayek et al. [18].

In addition, simple laboratory experiments are gaining interest for the evaluation of specific concepts for reactive transport codes. Lagneau [20] conducted column experiments to investigate the feedback of porosity changes on transport parameters in both diffusive and advective regimes. Porosity change was forced by the injection of a reactive solution, which triggered the replacement of a primary mineral phase by secondary mineral phases of larger molar volumes. The advective experiments consisted in the injection of a zinc sulfate solution into a porous medium consisting of calcite, which resulted in the formation of gypsum ($CaSO_{4(s)}\cdot 2H_2O$) and smithsonite ($ZnCO_{3(s)}$). In the diffusive system, the porous medium was replaced by portlandite ($Ca(OH)_2$), which, after reaction, was transformed to gypsum and zinc hydroxide ($Zn(OH)_2$). These experiments were used to test the feedback between chemistry and transport in the reactive transport code HYTEC. Similarly, Tartakovsky et al. [21] and Katz et al. [22] conducted mixing-induced calcite precipitation in porous media to test the validity of using the advection–dispersion reaction equation (ADRE) for describing pore-scale porosity clogging phenomena. The authors demonstrated the inappropriateness of using the ADRE for such a description. Tartakovsky et al. [21] proposed a modified equation of the ADRE to include transport mixing indices in the reaction terms that could account for highly non-uniform pore-scale concentration gradients and localized precipitation on the subgrid scale.

In addition to analytical solutions and laboratory experiments, numerical benchmarks are also used to test specific existing and new concepts of reactive transport codes. SeS Bench is an initiative for benchmarking subsurface environmental simulation methods with a current focus on reactive transport processes (Steefel et al. [23, 24] and references therein). Xie et al. [25] investigated the implementation of the Kozeny–Carman equation and Archie's law in reactive transport codes and evaluated the porosity changes due to mineral precipitation and dissolution. The benchmark considered different processes including advective–dispersive transport in saturated media, kinetically controlled mineral precipitation and dissolution leading to porosity changes, and aqueous complexation. Results from reactive transport codes (HP1, MIN3P-THCm, PFLOTRAN, CrunchFlow, and TOUGHREACT) were in good agreement, although some differences were observed for scenarios involving clogging which could be attributed to different implementations of the permeability–porosity and tortuosity–porosity relationships, the activity correction model, and numerical methods. A similar numerical benchmark involving the evaluation of transport parameters such as diffusivity and permeability due to porosity changes was also proposed by Cochepin et al. [26]. The authors forced the dissolution of portlandite followed by the precipitation of calcium oxalate due to the ingress of sodium oxalate in

a 2D setup. As the oxalate has a greater molar volume than portlandite, porosity clogging is forced with such a setup. Reactive transport codes (HYTEC and CRUNCH) that participated in the benchmark were in fairly good agreement. Discrepancies were explained by the different models used for describing the reactive surface area of precipitating and dissolving minerals. Although it was originally planned to also experimentally study this scenario, these plans were never realized.

We propose a reactive transport benchmark based on experiments by Poonoosamy et al. [27, 28] and Prasianakis et al. [29] with four levels of complexity. The benchmarked processes include kinetically controlled dissolution–precipitation reactions leading to porosity and, consequently, permeability and diffusivity changes. In this paper, we present and analyze the results of five established reactive transport codes (i.e., CORE^{2D}, MIN3P-THCm, OpenGeoSys-GEM, PFLOTRAN, and TOUGHREACT).

2 Benchmark problem setup

The experiment, on which the benchmark is based, is extensively described in Poonoosamy et al. [27]. Here, only the information that is important for the benchmark implementation is summarized. The experiment was conducted in a flow cell using the setup depicted in Fig. 1. It consists of a *reactive porous layer* (Q2) of celestite ($SrSO_4$) between two *inert porous layers* (Q1 and Q3) composed of quartz (SiO_2). The flow cell has dimensions of 0.1 m × 0.1 m × 0.01 m, and it contains several ports for fluid injection and sampling. The inlet and outlet positions were chosen to create an asymmetric flow field. Our numerical simulations are based on this setup.

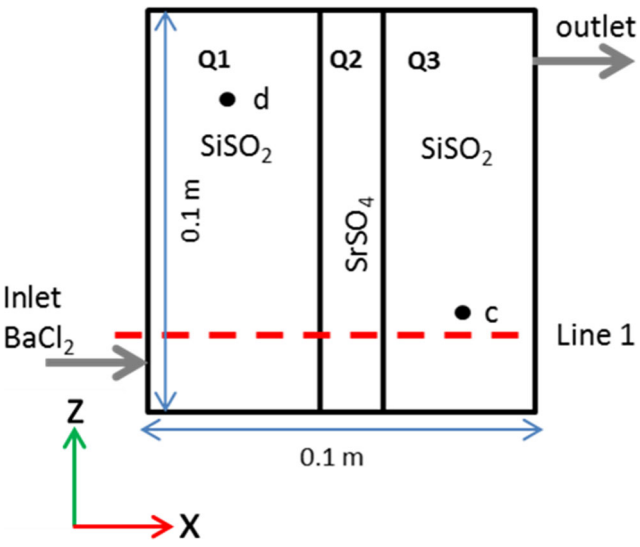

Fig. 1 Geometry of the numerical benchmark

In Table 1, we list the properties of the different regions shown in Fig. 1 (Q1, Q2, and Q3), as well as the fluid properties and initial conditions used for the numerical calculations. The ports "c" and "d," where samples were withdrawn, are located at (0.08 m, 0.02 m) and (0.02 m, 0.08 m), respectively.

Model results are compared at the locations "c" and "d" for solute concentrations versus time and along line 1 ($z = 0.01$ m) for mineral, porosity, and permeability profiles at selected times.

Four different benchmark cases with increasing complexity are defined. In *case 1*, we study flow with conservative mass transport. *Case 2* extends case 1 by considering density-driven flow with conservative mass transport. In *case 3*, we consider the dissolution and precipitation of mineral phases, leading to porosity changes. This case has two variants: *case 3a* with small porosity changes and *case 3b* with strong porosity changes. Finally, *case 4* extends case 3 by considering the formation of a $BaSO_4$–$SrSO_4$ solid solution. Table 2 provides additional information on the inlet and outlet conditions for the case studies. A detailed description of initial and boundary conditions for case studies 2, 3a, 3b, and 4 are provided in Tables 4, 5, 6, and 7, respectively, in Appendix A. For cases 3 and 4, density-driven flow induced by the injection of a concentrated $BaCl_2$ solution was ignored, because in most codes, the fluid density is not coupled to chemical reactions.

For all simulations performed using finite element codes (CORE^{2D}, OpenGeoSys-GEM), we considered a discretization of the square geometry in Fig. 1 by triangular or quadrilateral elements. For cases 1, 2, and 4, a nodal spacing distance of 1 mm was chosen, while for cases 3a and 3b, a more refined mesh was adopted, with a nodal spacing of 0.5 mm for OpenGeoSys-GEM. For finite volume codes (MIN3P-THCm, PFLOTRAN, TOUGHREACT), the domain was discretized into rectangular grid blocks with a nodal spacing of 1 mm, yielding a total number of 10,000 grid blocks.

2.1 Case 1: conservative mass transport

Here, we consider the injection of a non-reacting solution into the flow cell initially saturated with pure water. A conservative tracer of 3 g L^{-1} is injected at the inlet at a rate of 20 µL min^{-1} for 25 min (totaling 0.5 mL), followed by the inflow of the water without the tracer up to 24 h. The Q2 region, composed of $SrSO_4$, is assumed to be non-reactive in this case study.

The system was simulated for 24 h.

Table 1 Properties of the different regions of porous media

Characteristics	Q1	Q2	Q3
Length (m), cases 1, 2, and 3a	0.045	0.01	0.045
Length (m), cases 3b and 4	0.045	0.005	0.055
Initial porosity (w_0) (−), cases 1, 2, and 3a	0.34	0.33	0.40
Initial porosity (w_0) (−), case 3b	0.34	0.10	0.40
Initial porosity (w_0) (−) Case 4	0.34	0.40	0.40
Initial permeability, k_0 (m^2), cases 1, 2, and 3a	1.82×10^{-11}	1.8×10^{-14}	1.82×10^{-11}
Initial permeability, k_0 (m^2), case 3b	1.82×10^{-11}	5.0×10^{-16}	1.82×10^{-11}
Initial permeability, k_0 (m^2), case 4	1.82×10^{-11}	3.0×10^{-14}	1.82×10^{-11}
Dispersivity, α (m), cases 1 and 4	10^{-4}	10^{-4}	10^{-4}
Dispersivity, α (m), cases 2, 3a, and 3b	10^{-5}	10^{-5}	10^{-5}
Pore diffusion coefficient, D_p ($m^2\ s^{-1}$)	10^{-9}	10^{-9}	10^{-9}
Volume fraction of SiO_2, cases 1, 2, 3, and 4 (−)	0.66	0	0.60
Total volume fraction of $SrSO_4$ (−), case 1, 2, and 3a	0	0.67	0
Volume fraction of small $SrSO_4$ grains (−), case 3a		0.223	
Volume fraction of large $SrSO_4$ grains (−), case 3a		0.447	
Total volume fraction of $SrSO_4$ (−), case 3b (1 $SrSO_4$ grain size only)	0	0.90	0
Total volume fraction of $SrSO_4$ (−), case 4 (1 $SrSO_4$ grain size only)	0	0.60	0
Initial pH (fixed by initial chemical setup)	5.6	5.6	5.6

In the case of $CORE^{2D}$ and OpenGeoSys, dispersivity is isotropic, including the longitudinal and transversal dispersive length. In case 3a, the Q2 region is composed of bimodal grain size distribution of SrSO4 crystals (mixture of large and small grains)

2.2 Case 2: conservative mass transport coupled with density-driven flow

The injection of a highly concentrated solution of sodium chloride at a flow rate of 20 μL min^{-1} into the flow cell initially saturated with pure water is considered. The sodium chloride solution was amended with a 3×10^{-6} M conservative tracer (molar mass of 39.948 g mol^{-1}) for the first 25 min (totaling 0.5 mL). The injected solution is also saturated with respect to strontium sulfate. The calculation time is set to 24 h.

2.3 Case 3a: mineral dissolution and precipitation with small porosity changes

A highly concentrated solution of barium chloride ($BaCl_2$) is injected into the flow cell. The injection of $BaCl_2$ enhances the dissolution of $SrSO_4$ and causes barite ($BaSO_4$) to precipitate according to the following reaction:

$$Ba^{2+}_{(aq)} + SrSO_{4(s)} \rightarrow BaSO_{4(s)} + Sr^{2+}_{(aq)} \quad (1)$$

Table 2 Characteristics of the inlet and outlet

Characteristics	Case 1	Case 2	Case 3a	Case 3b	Case 4
Inlet ($x = 0$ m; $z = 0.00965$ m) length (m)	0.0033	0.0033	0.0033	0.0033	0.0033
Outlet ($x = 0.1$ m; $z = 0.0902$ m) length (m)	0.0033	0.0033	0.0033	0.0033	0.0033
Injection rate (μL min^{-1}) at inlet	20.0	20.0	20.0	20.0	10.0
NaCl concentration (mol L^{-1}) at inlet	NA	1.4	NA	NA	NA
$BaCl_2$ concentration (mol L^{-1}) at inlet	NA	NA	0.3	0.3	0.001
$SrCl_2$ concentration (mol L^{-1}) at inlet	NA	NA	NA	NA	0.099
Pressure at outlet (Pa)	101,325	101,325	101,325	101,325	101,325
Amount (mL) of dye tracer injected	0.5	0.5	NA	NA	NA
Concentration of dye tracer	3g L^{-1}	3×10^{-6} mol L^{-1}	NA	NA	NA
Modeling time duration (h)	24	24	300	200	600

NA not applicable

Porosity changes are likely to occur, given that $BaSO_4$ has a larger molar volume than $SrSO_4$. As a result, permeability and diffusivity will change.

The reactive layer Q2 has an initial porosity of 33% and is composed of two grain-sized populations of $SrSO_4$ (i.e., celestite 1 and celestite 2). Celestite 1 corresponds to $SrSO_4$ with a smaller grain size than celestite 2. Different kinetic rates of dissolution are used for these two grain-sized populations (see Section 3.2.4). The following reactive surface areas (per mineral volume unit) were attributed to the small and large crystals, respectively (20,000 m^2 $m^{-3}_{mineral}$ and 100 m^2 $m^{-3}_{mineral}$). We assumed no kinetic constraints on the precipitated barite ($BaSO_{4(s)}$) phase; i.e., thermodynamic equilibrium was assumed.

The simulation time is set to 300 h.

2.4 Case 3b: mineral dissolution and precipitation with strong porosity changes

Case 3b considers a reactive medium (Q2) of celestite with a lower initial porosity of 0.1. Due to the lower initial porosity, the injection of a highly concentrated $BaCl_2$ solution induces a stronger porosity decrease than in case 3a. The reactive medium is composed of celestite with a single grain-sized population. The reactive surface area ($a_{(SrSO_4)}$) is 20,000 m^2 $m^{-3}_{mineral}$.

The simulation time is set to 200 h.

2.5 Case 4: reactive transport involving the formation of a solid solution

Here, the reactive medium is composed of celestite with a single grain-sized population of 63–125 µm. The reactive surface area ($a_{(SrSO_4)}$) is 10,000 m^2 $m^{-3}_{mineral}$. A solution which composed of 0.099 mol L^{-1} $SrCl_2$ and 0.001 mol L^{-1} $BaCl_2$ is injected at the inlet at a flow rate of 10 µL min^{-1}.

The simulation time is set to 600 h.

3 Mathematical model formulations and numerical implementations

All codes implemented the same flow and advection–dispersion equations for porous media. The transport equation of a chemical component is given as [24]

$$\frac{\partial C_i}{\partial t} = \nabla (D_i \nabla C_i) - \nabla \left(\frac{\vec{q}}{w} C_i \right) + Q_i \tag{2}$$

where C_i denotes the molar concentration of the ith species, D_i is the diffusion dispersion of species assumed to take the same value for all solutes, w is the porosity, $\vec{q}$ is the Darcy velocity (m s^{-1}), and Q_i is the source/sink term. D_i can be reduced to the following scalar form: $D_i = \alpha \left| \frac{\vec{q}}{w} \right| + D_e$, where D_e is the effective diffusion (m^2 s^{-1}) coefficient assumed to take the same value for all solutes and α (m) is the dispersivity of the porous medium. The choice of isotropic (transversal dispersion tensor = longitudinal dispersion tensor) or anisotropic (transversal dispersion tensor ≠ longitudinal dispersion tensor) dispersion is usually imposed by the code.

The thermodynamic data (standard Gibbs energy of formation (kJ mol^{-1})) of aqueous, gaseous, and solid species considered in our chemical system and the molar volumes (m^3 mol^{-1}) are given in Table 3.

3.1 Numerical codes

3.1.1 CORE^{2D}

CORE^{2D} V5 is a code for transient saturated and unsaturated water flow, heat transport, and multicomponent reactive solute transport under both local chemical equilibrium and kinetic conditions in heterogeneous and anisotropvic media. It can handle microbial processes and abiotic reactions including acid–base, aqueous complexation, redox, mineral dissolution–precipitation, gas dissolution–exsolution, cation exchange, and surface complexation. Hydraulic parameters may change in time due to mineral precipitation–dissolution reactions. The flow and transport equations are solved with Galerkin triangular finite elements and an Euler scheme for time discretization [30, 31]. The chemical formulation is based on the ion association theory and uses an extended version of the Debye–Hückel (B-dot) equation for activity coefficients of aqueous species. CORE^{2D} V5 is based on the sequential iteration approach to solve chemical reactive solute transport. Iterations are repeated until prescribed convergence criteria are attained [30]. The code has been widely used to model laboratory and in situ experiments [32–37], to model the interactions of corrosion products and bentonite [38], and to evaluate the long-term geochemical evolution of repositories in granite and clay [39, 40].

3.1.2 MIN3P-THCm

MIN3P-THCm is a multicomponent reactive transport code, specifically designed for simulating flow and reactive transport processes in variably saturated media, including density effects. The code uses the global implicit method implemented using the direct substitution approach (DSA) for solution of the multicomponent advection–dispersion equation and biogeochemical reactions [41]. Spatial discretization is performed based on the finite volume method, facilitating simulations in one, two, and three spatial dimensions.

Table 3 Thermodynamic database of aqueous, gaseous, and solid species present under standard conditions for OpenGeoSys-GEM

Phase	Component	Standard Gibbs energy of formation, ΔG_f^0 (kJ mol^{-1})	Molar volume (10^{-5} m^3 mol^{-1}) under standard conditions
Aqueous	$Ba(CO_3)$	−1104.251[a]	−1.1798542[c]
	$Ba(HCO_3)^+$	−1153.325[a]	1.917225[c]
	$Ba(SO_4)$	−1320.652[a]	0.818138[c]
	Ba^{2+}	−560.782[b]	−1.2901389[b]
	$BaOH^+$	−721.077[a]	0.91585235[b]
	$Sr(CO_3)$	−1107.830[a]	−1.5228401[c]
	$Sr(HCO_3)^+$	−1157.538[a]	1.4082323[c]
	$Sr(SO_4)$	−1321.366[a]	0.50248447[c]
	Sr^{2+}	−563.836[b]	−1.7757955[b]
	$SrOH^+$	−725.159[a]	0.70988636[b]
	CO_2	−386.015[a]	3.2806681[d]
	CO_3^{-2}	−527.982[a]	−0.60577246[b]
	HCO_3^-	−586.940	2.4210897[b]
	Cl^-	−131.290[a]	1.7340894[b]
	H_2	17.729[a]	2.5264358[d]
	O_2	16.446[a]	3.0500889[d]
	HSO_4^-	−755.805[a]	3.484117[b]
	SO_4^{-2}	−744.459	1.2917656[b]
	OH^-	−157.27[a]	−0.470784[b]
	H^+	0.00	0.00
	H_2O	−237.18138[c]	1.807[c]
Gaseous	CO_2	−394.393[a]	2478.9712[e,f]
	H_2	0.00[a]	2478.9712[e,f]
	O_2	0.00[a]	2478.9712[e,f]
Solid	$Ba(CO_3)$	−1137.634[a]	5.03[c]
	$Ba(SO_4)$	−1362.152[a]	5.21[g]
	Quartz	−854.793[a]	2.2688[g]
	$Sr(CO_3)$	−1144.735[a]	3.901[g]
	$Sr(SO_4)$	−1346.15[a]	4.625[g]

The standard Gibbs energies of formation (kJ mol^{-1}) were calculated from the equilibrium constants reported in "a" and "b" corresponding to Hummel et al. [70] and Shock et al. [71], respectively, and "c," "d," "e," "f," and "g" are references from Sverjensky et al. [72], Shock et al. [73], Wagman et al. [74], Kelley [75], and Helgeson et al. [76], respectively

Advective transport terms can be described by upstream weighting, centered spatial weighting, or using a flux limiter technique to minimize numerical dispersion. Implicit time weighting is employed, which allows using large time steps for problems that are strongly affected by the water–rock interaction, without loss of accuracy. The highly non-linear and coupled reactive transport equations are linearized using Newton's method. MIN3P-THCm includes a generalized framework for kinetically controlled reactions, which can be specified through a database along with equilibrium processes. The general kinetic formulation includes intra-aqueous and dissolution–precipitation reactions in addition to geochemical equilibrium expressions for hydrolysis, aqueous complexation, oxidation–reduction, ion exchange, surface complexation, and gas dissolution–exsolution reactions [23].

MIN3P-THCm (version 1.0.440) was used in our simulations.

3.1.3 OpenGeoSys-GEM

The fluid flow and mass transport equations are solved by OpenGeoSys based on a standard finite element formulation, and the chemical processes by the GEMS3K kernel code of GEM-Selektor V3 [42]. The coupling of these two codes is referred to as OpenGeoSys-GEM, and its capabilities are described in Shao et al. [43] and Kosakowski and Watanabe [44]. Mass transport and

chemical reactions are solved in a sequential non-iterative approach (SNIA); i.e., the transport and reaction equations are solved separately in a sequential manner without the iteration between them.

The GEM approach as implemented in GEMS3K consists of calculating the equilibrium state of a chemical system via minimization of its Gibbs free energy. The minimization is constrained by mass balance equations where the given total amounts of chemical elements are conserved. An additional charge balance equation is also imposed to enforce the electro-neutrality condition of the system. The equilibrium state calculated by GEMS3K provides the mole amounts of every species in the system and the composition of all solid, liquid, or gaseous phases [45]. In addition, other chemical quantities such as species activities or saturation indices that are needed for the calculation of kinetic rates of mineral dissolution are provided.

OGS5 (version 5) coupled to Gems Selector V3 was used for modeling.

3.1.4 PFLOTRAN

PFLOTRAN [46] is a massively parallel subsurface flow and reactive transport code, designed to run on large computing architectures as well as workstations and laptops. Parallelization is achieved through domain decomposition using the PETSc libraries. PFLOTRAN can handle different discretization schemes including structured (Cartesian, cylindrical) and unstructured (implicit and explicit) grids. Currently, PFLOTRAN can handle a number of subsurface processes including Richards' equation, two-phase flow involving supercritical CO_2, and reactive transport including aqueous complexing, sorption, mineral precipitation and dissolution, and Monod-type biochemical reactions. Reactive transport equations are solved using a fully implicit Newton–Raphson algorithm. An elastic geomechanical model is also implemented. PFLOTRAN can run multiple input files and multiple realizations simultaneously on one or more processor cores per run which is useful for sensitivity studies and quantifying model uncertainties. More information about the PFLOTRAN development can be obtained from the project website at www.pflotran.org.

PFLOTRAN (version 2015) was used in our simulations.

3.1.5 TOUGHREACT

A detailed description of TOUGHREACT and its capabilities is given in [47] and [23]. TOUGHREACT was developed by coupling geochemical reactions to the TOUGH2 V2 family of multiphase flow simulators [48]. The primary governing equations for multiphase fluid and chemical transport are derived from the principle of mass and energy conservation. The mass and energy balance equations are solved implicitly by Newton–Raphson iterations. Space discretization involves an unstructured finite volume scheme (integral finite differences). Reactive transport is solved by an operator-splitting approach that can be either iterative or non-iterative. Reactive processes considered include aqueous and surface complexation, ion exchange, mineral precipitation–dissolution, microbial mediated biodegradation, and gas exsolution–dissolution.

TOUGHREACT (version TOUGHREACT V3.0.-OMP) was used in our simulations

3.2 Model formulations

3.2.1 Density-driven flow and transport

Four codes, namely MIN3P-THCm, OpenGeoSys-GEM, PFLOTRAN, and TOUGH2, allow the modeling of flow influenced by the density of the fluid.

In OpenGeoSys-GEM, PFLOTRAN, and TOUGH2, the Boussinesq approximation is considered; i.e., the density variation is neglected in the mass conservation equation of the fluid phase. Density variations are included by the buoyancy term of the Darcy equation only. For variable-density flow in porous media, the Darcy velocity ($\mathbf{q}$) (m s^{-1}) is given as

$$\mathbf{q} = -\frac{k}{\mu}\left(\nabla p - \rho \mathbf{g}\right) \tag{3}$$

where k is the permeability (m^2), μ is the dynamic viscosity (Pa s) of the fluid, ∇p (Pa) is the pressure gradient, ρ is the density of the fluid (kg m^{-3}), and $\mathbf{g}$ is the gravity vector (m s^{-2}).

In OpenGeoSys-GEM, the density of the aqueous phase is calculated by GEMS3K, which is dependent on its molar composition. This is done by calculating the partial molar volumes of each aqueous species at the temperature and pressure of interest. Then, the products of these partial molar volumes with the corresponding molar amounts of the aqueous species are summed up in order to obtain the overall volume of the aqueous phase. The total mass of the aqueous phase divided by this volume gives the density of the aqueous phase. This density is updated after each chemical equilibrium calculation and passed along to the fluid flow solver for calculation of the next time step.

In PFLOTRAN, the density of the brine is calculated from empirical relations described in [49].

TOUGHREACT does not consider changes in fluid density as a function of the chemical composition. For this benchmark, flow influenced by density was therefore simulated using TOUGH2-EOS7 [48]. This equation of state represents the fluid phase as a mixture of water and brine, and the salinity is described by means of the brine mass fraction (X_b). In doing so, fluid density (ρ) is

interpolated from the values of the water (ρ_w) and brine end-members (ρ_b)

$$\frac{1}{\rho} = \frac{1 - X_b}{\rho_w} + \frac{X_b}{\rho_b} \tag{4}$$

For the simulation of case 2, the density of the brine was set to 1057 kg m^{-3}. The diffusive flux (J_D) is calculated as

$$J_D = w D \rho \frac{\Delta X_b}{\Delta X} \tag{5}$$

where w is the porosity, D (m^2 s^{-1}) is the diffusion coefficient, ρ (kg m^{-3}) is the fluid density, and $\frac{\Delta X_b}{\Delta X}$ is the gradient of the brine mass fraction (i.e., concentration gradient). Equation 3 demonstrates that in TOUGH2-EOS7, the effective diffusion coefficient is not only a function of porosity and the intrinsic diffusion coefficient, but it also depends on the fluid density. As the fluid density is changing with time and space, the effective diffusion coefficient is not constant throughout the simulation.

MIN3P-THCm implemented the fluid flow equation considering the density-driven flow without the Boussinesq approximation [50]. For saturated porous media, the equation is derived as

$$\frac{\partial}{\partial t}(\rho w) - \nabla \cdot (\rho \mathbf{q}) = \rho Q_a \tag{6}$$

where w is the porosity and Q_a represents fluid sources/sinks.

The aqueous phase fluid density is computed as a function of temperature and chemical concentrations according to

$$\rho = \rho_0 + \Delta\rho_c + \Delta\rho_T \tag{7}$$

where ρ_0 is the reference density (e.g., density of pure water at 25 °C). $\Delta\rho_c$ and $\Delta\rho_T$ represents the density changes due to concentration and temperature, respectively.

In MIN3P-THCm, there are two approaches for calculation of the fluid density. A commonly employed empirical approach treats fluid density change as a linear function of total dissolved solids (TDS) [50–54]

$$\Delta\rho_c = \frac{\partial \rho}{\partial \mathrm{TDS}} \mathrm{TDS} \tag{8}$$

where $\frac{\partial \rho}{\partial \mathrm{TDS}}$ is assumed to be constant. Reported values for the constant $\frac{\partial \rho}{\partial \mathrm{TDS}}$ range between 0.688 and 0.7125 for geochemical modeling of seawater–freshwater interactions [51–55]. For the case 2 calculation, the constant was set to 0.7125 [50, 55].

The linear relationship between density and TDS is typically assumed when NaCl dominates the salinity (e.g., seawater). However, the presence of $CaCl_2$-enriched brines requires a model for density calculations that considers the elemental composition of the fluids (e.g., [56]). MIN3P-THCm also includes an approach based on the Pitzer ion interaction model [57, 58] for the computation of $\Delta\rho_c$. The model calculates the solution density based on the molar volume of solutes and the excess volume of a multicomponent electrolyte solution due to ion interactions in highly saline solutions. A detailed description of the formulation for fluid density as a function of solution composition is provided in Appendix B.4 of Bea et al. [59].

3.2.2 Porosity, diffusivity, and permeability

As a result of dissolution–precipitation reactions, porosity changes occur. Transport properties of the medium, such as effective diffusion coefficients (D_e) and the permeability (k_s), are commonly parameterized as a function of porosity.

For the dependence of the effective diffusion coefficient on porosity, we used a simplified Archie relation [60]

$$D_e = D_p w^m \tag{9}$$

where D_p (m^2 s^{-1}) is the pore diffusion coefficient, w (−) is the porosity, and m (−) is an empirical coefficient. In this study, m was set to 1.

For CORE^{2D}, TOUGHREACT, and MIN3P-THCm, changes of permeability, k_s (m^2), with porosity are calculated from the Kozeny–Carman relation [61]

$$k_s = k_0 \left(\frac{1-w_0}{1-w}\right)^2 \left(\frac{w}{w_0}\right)^3 \tag{10}$$

For OpenGeoSys-GEM and PFLOTRAN, changes of permeability, k_s (m^2), with porosity are given by the modified Kozeny–Carman equation

$$k_s = k_0 \left(\frac{w}{w_0}\right)^3 \tag{11}$$

where k_0 (m^2) is the initial permeability and w and w_0 are the current and initial porosities, respectively.

3.2.3 Activity corrections

In all participating codes, the activity coefficients for all dissolved species (γ_j) are calculated according to the extended Debye–Hückel equation [62]. A detailed description is reported in Wagner et al. [45]. Equation 12 relates the activity coefficients of an aqueous ion to its charge (Z_j) and ionic strength (I)

$$\log_{10}\gamma_j = \frac{-A_\gamma Z_j^2 \sqrt{I}}{1 + \dot{a} B_\gamma \sqrt{I}} + b_\gamma I \tag{12}$$

where $\dot{a}$ (in Å) is an average distance of the approach of two ions of opposite charges and b_γ is a semi-empirical coefficient, either individual for a given electrolyte or common for all aqueous species. $\dot{a}$ and b_γ were set to 3.72

and 0.064, respectively, for all the ionic species [62]. A_γ and B_γ are temperature-dependent coefficients set to 0.5114 and 0.3288, respectively, at a temperature of 25 °C [63]. Activity coefficients (γ_j) for neutral species (dissolved gases) and water were set to unity. For the simulation of case 2 using the Pitzer ion interaction approach of MIN3P-THCm, Pitzer equations [64, 65] were adopted.

3.2.4 Kinetics of precipitation and dissolution reactions of minerals

In addition to the transport of $BaCl_2$ and chemical reactions, there is transformation from celestite to barite, and thus, the porosity evolution is also influenced by reaction kinetics.

In our simulations, barite was assumed to precipitate instantaneously (very fast kinetics) and only the dissolution kinetics of celestite was taken into account. The dissolution rate of celestite dm/dt (mol s^{-1} m_{bulk}^{-3}) at pH 5.6 (pH of the experiment) is calculated based on the equation given in Palandri and Kharaka [66] with parameters from Dove and Czank [67].

$$\frac{dm}{dt} = -SAk^{\circ}(1-\Omega) \tag{13}$$

where SA (m^2 m_{bulk}^{-3}) is the reactive surface area of the celestite mineral phase, $k^{\circ}=10^{-5.66}$ mol m^{-2} s^{-1} is the dissolution rate constant at 298.15 K, and Ω is the ratio between the ion activity product of the mineral and its equilibrium constant.

In our simulations, a very simple reactive surface area model was chosen

$$SA = \frac{V}{V_{bulk}} \times a \tag{14}$$

where V (m^3) and V_{bulk} (m^3) are the volume of the mineral and the total bulk volume, respectively, and a (m^2 $m_{mineral}^{-3}$) is the mineral's specific surface area (i.e., surface area per volume of the mineral phase). The reactive surface area of each mineral phase was calculated using Eq. 14.

The reactive surface area is updated during the simulations as mineral volume fractions change due to dissolution and precipitation reactions. The update of the surface area is formulated as follows:

$$SA_{(t)} = SA_{(0)} \frac{V_t}{V_0} \tag{15}$$

where $SA_{(0)}$ and V_0 are the initial surface area and mineral molar volume fraction, respectively, and $SA_{(t)}$ and V_t are the surface area and volume fraction at time t, respectively.

The reaction rates as described above are the formulations that are used by OpenGeoSys-GEM whereby reaction rate is defined per bulk volume. However, in other codes, e.g., TOUGHREACT, reaction rates are per mass of solvent, that is the reactive surface area; reaction rate constants are usually given in m^2 $kg_{H_2O}^{-1}$ and mol kg^{-1} m^{-2} s^{-1}, respectively (c.f. Section 3.2.5), and therefore, the conversions were made such that the same reaction rates are used in all the reactive transport codes.

3.2.5 Solid solution

A solid solution phase is defined as a mixture of solids forming a homogeneous crystalline structure. The thermodynamics of solid solutions has been described in detail by Bruno et al. [68]. Solid solution formation is considered in case 4, and only OpenGeoSys-GEM and TOUGHREACT can deal with the calculation of solid solutions.

The Gibbs energy of an ideal solid solution (composed of n components) can be split into the weighted Gibbs energy of pure end-members ($G_i^0 X_i$) and the ideal Gibbs energy of mixing (ΔG_{mix}^{id}) (J)

$$\begin{aligned}\Delta G_{total}^{real} &= \sum_{i=1}^{n} G_i^0 X_i + \Delta G_{mix}^{id} = \sum_{i=1}^{n} G_i^0 X_i + \Delta H - T\Delta S \\ &= \sum_{i=1}^{n} G_i^0 X_i + RT(X_{BaSO_4}\ln X_{BaSO_4} + X_{SrSO_4}\ln X_{SrSO_4})\end{aligned} \tag{16}$$

where ΔH is the enthalpy of mixing (zero for ideal solid solutions), ΔS is the entropy of mixing, T is the temperature (K), R is the gas constant, and X_i is the mole fraction of end-member i.

Because the formation of a solid solution increases the disorder of the crystal lattice by the random substitution of ions, the entropy term of mixing is always positive. This decreases the Gibbs energy of the ideal solid solution and favors the formation of the solid solution compared to the formation of pure phases. Figure 2 shows the Lippmann diagram (total solubility product ($\sum\prod$) versus mole fractions of aqueous Ba^{2+} and solid $BaSO_4$) for an ideal solid solution of $BaSO_4$ and $SrSO_4$. The total solubility product ($\sum\prod$) is defined as the sum of the partial activity products contributed by the individual end-members of the solid

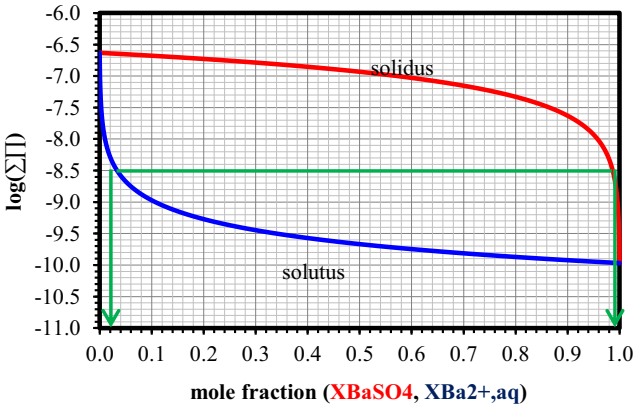

Fig. 2 Lippmann diagram of an ideal solid solution of $SrSO_4$ and $BaSO_4$

solution. In thermodynamic equilibrium, the total activity product ($\sum \prod_{eq}$) expressed as a function of the solid solution composition yields the solidus curve. Similarly, the solutus curve expresses $\sum \prod_{eq}$ as a function of the aqueous solution composition. Equations for the derivation of the solutus and solidus curves are given in Appendix B. Figure 2 shows that the formation of a $BaSO_4$–$SrSO_4$ solid solution is only possible when the concentration of Ba^{2+} in solution is relatively low (indicated by the arrows). A molar aqueous fraction of Ba^{2+} ($X_{Ba^{2+},aq}$) above 0.05 will result in the precipitation of pure barite. Although the solid solution of $BaSO_4$–$SrSO_4$ occurs in nature, the large difference in the solubility product of the end-members ($\Delta \log K \approx 3.4$) renders its formation difficult under laboratory conditions. To make case 4 as realistic as possible, the injection of a solution consisting of a mixture of Ba^{2+} and Sr^{2+} (with respective molar fractions of 0.01 and 0.99) was considered to trigger the formation of a solid solution (Table 2).

In GEMS, the Gibbs energy of mixing is considered in the evaluation of equilibrium concentrations.

In TOUGHREACT, the ideal solid solution model is only available for minerals that react under kinetic constraints.

The overall precipitation rate of the solid solution (r_{ss}) is the sum of the precipitation rates of the two end-members [69].

$$r_{ss} = r_{SrSO_4} + r_{BaSO_4} \tag{17}$$

The precipitation rates r_{SrSO_4} and r_{BaSO_4} of the end-members are calculated according to

$$r_{SrSO_4} = A_{ss} k_{ss} \left(1 - \frac{Q_{SrSO_4}}{K_{SrSO_4}}\right) + A_{ss} k_{ss} . (x_{SrSO_4} - 1) \tag{18}$$

$$r_{BaSO_4} = A_{ss} k_{ss} \left(1 - \frac{Q_{BaSO_4}}{K_{BaSO_4}}\right) + A_{ss} k_{ss} . (x_{BaSO_4} - 1) \tag{19}$$

where A_{ss} ($m^2\ kg_{H_2O}^{-1}$) refers to the reactive surface area of the solid solution; k_{ss} (mol kg^{-1} m^{-2} s^{-1}) is the reaction rate constant of the solid solution; Q_{SrSO_4} and Q_{BaSO_4} are the ion activity product of the $SrSO_4$ and $BaSO_4$ minerals, respectively; K_{SrSO_4} and K_{BaSO_4} are the corresponding equilibrium constants; and x_{SrSO_4} and x_{BaSO_4} are the mole fractions of the precipitating end-members. The first terms in Eqs. 18 and 19 refer to the precipitation of the end-members as pure minerals (i.e., maximum rate). The second terms ensure that the precipitation rates of the end-members decrease linearly with decreasing mole fractions (as $x_{BaSO_4} - 1 < 0$).

To ensure that the volume ratios of these end-members reflect the fluid composition, x_{SrSO_4} and x_{BaSO_4} are calculated according to

$$x_{SrSO_4} = \frac{Q_{SrSO_4} / K_{SrSO_4}}{Q_{SrSO_4} / K_{SrSO_4} + Q_{BaSO_4} / K_{BaSO_4}} \tag{20}$$

$$x_{BaSO_4} = \frac{Q_{BaSO_4} / K_{BaSO_4}}{Q_{SrSO_4} / K_{SrSO_4} + Q_{BaSO_4} / K_{BaSO_4}} \tag{21}$$

In order to get the saturation index of the solid solution that is very close to zero within Q2, which is calculated by OpenGeoSys-GEM, the corresponding surface area (A_{ss}) and rate constant (k_{ss}) were set to 5957 $m^2\ kg_{H_2O}^{-1}$ (10,000 $cm^2\ g_{mineral}^{-1}$) and 1×10^{-5} mol kg^{-1} m^{-2} s^{-1}, respectively, to ensure fast precipitation.

4 Results

4.1 Case 1

Case 1 considers the injection of a non-reacting solution into a porous medium saturated with water. The flow field is visualized by the addition of a tracer pulse at the inlet. The temporal tracer profiles are shown in Fig. 3. At the beginning of the simulation, concentric circles of the tracer are observed. The circles get slightly distorted as the fluid moves towards the region of lower permeability (celestite layer, Q2) as shown by the contour plots after 8 h. The simulated tracer profiles of $CORE^{2D}$, MIN3P-THCm, OpenGeoSys-GEM, PFLOTRAN, and TOUGHREACT are visually in good agreement (only the tracer profile of MIN3P-THCm is presented below).

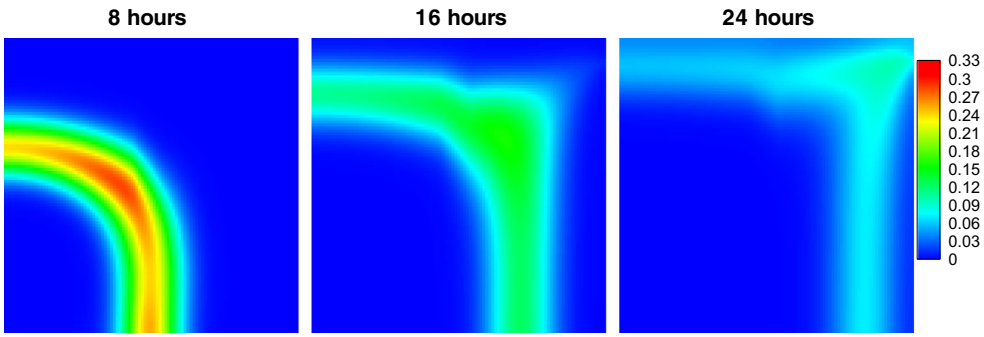

Fig. 3 Temporal tracer profile produced by MIN3P-THCm. A scale ranging from 0 to 0.33 g L^{-1} is used here for all temporal profiles (case 1)

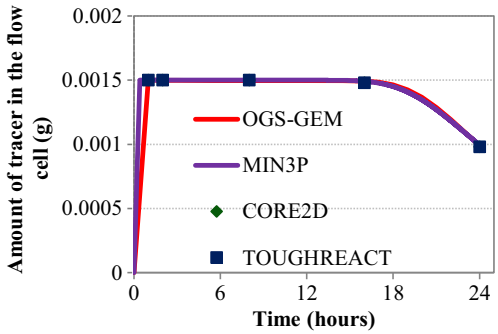

Fig. 4 The evolution of the total tracer mass (**g**) in the flow cell with time (case 1)

The time evolution of the mass of tracer in the flow cell is shown in Fig. 4. For the first 16 h, the amount of tracer mass present inside the flow cell is constant. Afterwards, there is a constant decrease $\sim -1.0 \times 10^{-4}$ g h^{-1} (-2.8×10^{-8} g s^{-1}) as the tracer is being removed from the domain at the outlet. The different codes produced the same result.

In addition, the calculated breakthrough curves of the tracer at ports "c" and "d" are shown in Fig. 5. In the case of OpenGeoSys, both triangular and quadrilateral mesh discretizations were tested. Both resulted in the same tracer distribution profiles.

The simulated tracer nodal concentrations of MIN3P-THCm, TOUGHREACT, and PFLOTRAN differ from those produced by CORE^{2D} and OpenGeoSys. Although the reason for these discrepancies could not be fully confirmed, it is likely that differences in model discretization methods are responsible.

Figure 6 compares the spatial differences in the magnitude of velocities in the flow cell produced by OpenGeoSys and TOUGHREACT. The velocities of OpenGeoSys were used as reference for the calculation of the relative difference in velocity magnitude. The most significant differences in velocity magnitude are observed at the inlet, the outlet, and the boundaries of the Q2 region. This results in differences in the spatial concentration of the tracer (Fig. 7).

A difference in the implementation of diffusive–dispersive transport was found. For OpenGeoSys and CORE^{2D}, the longitudinal and transversal dispersivity was set to the same value. In Min3P, the dispersion length is accounted using Eq. 9 in Mayer et al. [41] whereby longitudinal and transversal dispersivity was set to the same value of 10^{-5} m, resulting in a transversal term only. On the other hand, dispersive transport is not accounted for in TOUGHREACT. In the presented results from PFLOTRAN, only longitudinal dispersion was considered. Test calculations with PFLOTRAN using only longitudinal dispersion and the combination of transverse and longitudinal dispersion showed insignificant differences.

Last but not least, the intrinsic properties of the finite element and finite volume methods in solving the ADR equation might result in different values for numerical dispersion and influence the breakthrough curves. The effect of grid discretization for FE codes was tested and indicated that numerical dispersion is reduced for finer grids. The results from calculations with CORE^{2D} are given in Fig. S1A in the Supplement S1.

Overall, the breakthrough curves indicate that the evolution of the system is consistently described by all five codes, showing the maximum peaks between 18.5 and 19.4 h for port "c" and between 14.4 and 14.6 h for port "d."

4.2 Case 2

Case 2 considers the injection of a non-reacting saline solution into a porous medium initially filled with a fluid of lower density. This induces a transient flow regime, typical for density-driven flow. In the long term, the flow converges again to the stationary flow regime of case 1. The tracer profiles shown in Fig. 8 allow the visualization of the evolution of a tracer pulse, which was injected together with the $BaCl_2$ solution at the beginning of the experiment. This case was solved by the reactive transport codes MIN3P-THCm, PFLOTRAN, TOUGH2, and OpenGeoSys-GEM.

Figure 9 compares the fluid densities at ports "c" and "d" of MIN3P-THCm, OpenGeoSys, PFLOTRAN, and TOUGHREACT. In OpenGeoSys-GEM, the density of the fluid is calculated as the ratio of mass to volume of the fluid. The volume of the fluid is calculated based on the aqueous species present and the molar volumes of these aqueous

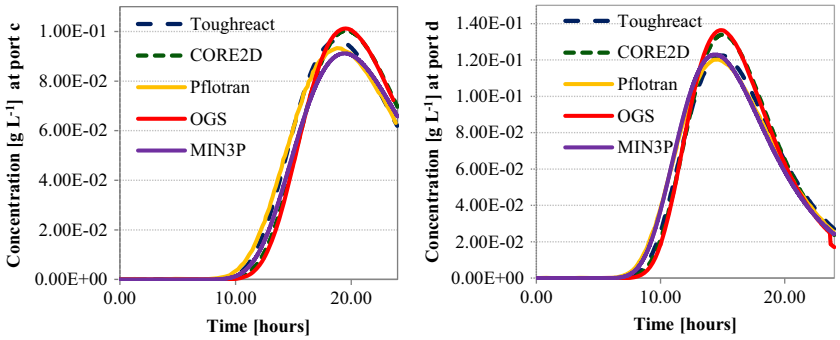

Fig. 5 Concentration of tracer measured at ports "c" (left) and "d" (right) at different times (case 1)

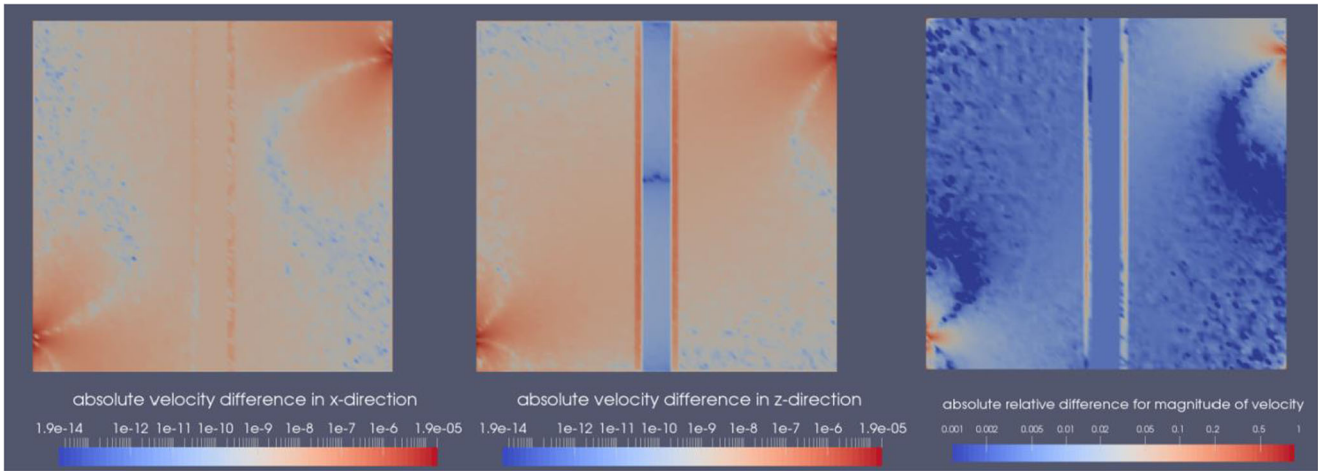

Fig. 6 Absolute velocity differences in x-direction and z-direction and magnitude of velocity (from left to right) between OpenGeoSys and TOUGHREACT (case 1)

species. As such, the volume of the fluid increases as salinity increases. The densities calculated by PFLOTRAN using the empirical relationship by Batzle and Wang [49] and by OpenGeoSys-GEM are in qualitatively good agreement. MIN3P-THCm calculated case 2 using both the empirical and the Pitzer ion interaction approaches, and the results are very similar. The calculated fluid density using the Pitzer ion interaction approach is slightly lower than that using the empirical approach (Fig. 9). The maximum relative differences in fluid density calculated using both approaches are 0.28% and 0.16% at ports "c" and "d," respectively.

The fluid density correlates with the NaCl concentration. The NaCl breakthrough at the ports "c" and "d" showing similar trends as the fluid density (in Fig. 9) is, thus, not presented. The calculated NaCl concentrations (fluid densities) calculated by TOUGH2 for ports "c" and "d" differ from those calculated by PFLOTRAN and OpenGeoSys-GEM. As mentioned earlier, in TOUGH2, the effective diffusion coefficient is not only a function of porosity and intrinsic diffusion coefficient, but it also depends on the density of the fluid. The effective diffusion coefficient is consequently not constant throughout the experiment. The diffusion coefficient used for the calculations with TOUGH2 was set to 3×10^{-9} m^2 s^{-1} in order to approximate the constant value used by the other codes.

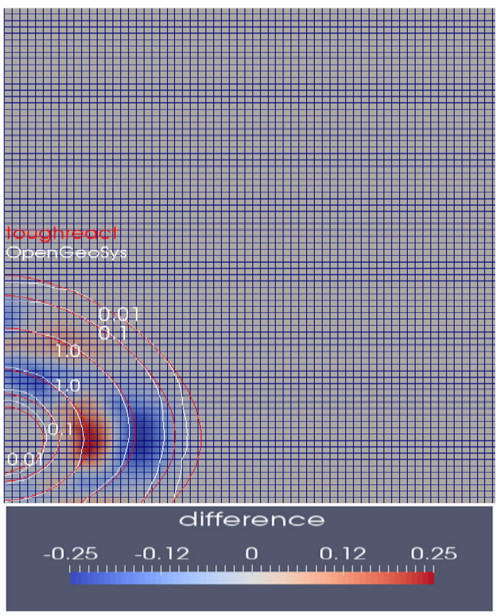

Fig. 7 Difference in tracer distribution between TOUGHREACT and OpenGeoSys after 1 h of fluid injection (case 1)

The breakthrough curves of NaCl (fluid density) at ports "c" and "d" of MIN3P-THCm, OpenGeoSys-GEM, and PFLOTRAN in Fig. 9 show a similar trend. A higher dispersion is observed with OpenGeoSys-GEM. A refined spatial discretization and the Crank–Nicolson scheme were tested for OpenGeoSys-GEM, but similar results were obtained. As in case 1, the differences between the breakthrough curves can be explained by a difference in the implementation of diffusive–dispersive transport. With OpenGeoSys-GEM, both the longitudinal and transverse dispersive lengths of 1×10^{-5} m were considered; with PFLOTRAN, the longitudinal dispersive length of 1×10^{-4} m was used, and with MIN3P-THCm, the transverse dispersive length of 1×10^{-5} m.

4.3 Case 3a

Case 3a extends case 1 by considering dissolution and precipitation of minerals that change the porosity and permeability (and the effective diffusion coefficient) in the flow cell. When a concentrated $BaCl_2$ solution reaches the reactive layer Q2, the dissolution of celestite ($SrSO_4$) is triggered and barite ($BaSO_4$) precipitates. Figure 10 shows

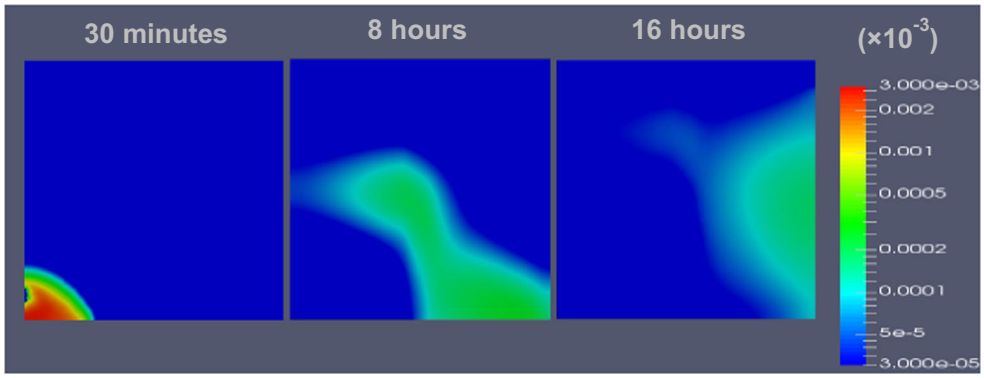

Fig. 8 Temporal tracer profiles produced by OpenGeoSys-GEM. The temporal profiles are mapped with a log scale with 3×10^{-11} mol L^{-1} and 3×10^{-6} mol L^{-1} as minimum and maximum, respectively (case 2)

the total amounts of $BaSO_4$ and $SrSO_4$ in the flow cell with time, which change due to either mineral dissolution or precipitation. During the first 150 h, dissolution of $SrSO_4$ at a constant rate of 0.2 mmol per h is observed. After 150 h, this dissolution rate slows down. Similarly, the total amount of precipitated barite increases during the first 150 h and slowly builds up to 0.043 mol at 300 h. The initial fast precipitation of barite during the first 150 h results from the dissolution of the smaller celestite particles (Cls 1). As the smaller celestite grains are consumed, aqueous SO_4^{2-} is supplied by the dissolution of larger grains of celestite (Cls 2), which is much slower due to its lower reactive surface area.

Differences in the total mineral dissolution and precipitation calculated by the five codes are negligible. The variation in flow velocities, as observed in case 1, does not have a significant impact on the total amount of minerals that precipitated and dissolved in the flow cell. This is because the variation in the flow field might results in small differences in the spatial distribution of ions but, in this case, very little impact on the total amount of mineral that was dissolved or precipitated in the flow cell.

Figure 11 compares the concentrations of major aqueous species across line 1 (Fig. 1) at 150 h and 300 h. Overall, the simulated concentrations match well although minor deviations are observed at greater distances from the inlet. These differences may be related to several reasons including differences in the implementation of diffusive–dispersive transport (as reported for case 1), variations in the implementation of transport schemes, differences in time stepping, small deviations in databases due to the use of different components, and differences in coupling schemes between transport and reactions.

The transformation of celestite to barite involves a volume increase of about 12%. The resulting porosity decrease and associated permeability changes are shown in Fig. 12. The porosity changes due to mineral transformation calculated by $CORE^{2D}$, MIN3P-THCm, OpenGeoSys-GEM, PFLOTRAN, and TOUGHREACT are the same. The associated changes in permeability simulated by the reactive transport codes due to the small porosity decrease (6%) are in good agreement. According to Fig. 12, for a porosity of 0.3 after 300 h, a permeability of 1.3×10^{-14} m^2 was calculated for $CORE^{2D}$, MIN3P-THCm, and TOUGHREACT and 1.4×10^{-14} m^2 was calculated for PFLOTRAN and OpenGeoSys-GEM. The evaluated difference in permeability is roughly 10% for a porosity decrease to 0.3 which what is expected if Eqs. 10 and 11 are applied for a porosity change from 0.33 to 0.30.

There are also small deviations between the porosity and permeability at the interfaces to the reactive layer Q2 ($x = 0.045$ m and $x = 0.055$ m) which are explained by the different spatial discretizations used by the codes and the processing of the results using the software ParaView (www.paraview.org/). There are difficulties in comparing the results of the different codes, e.g., generating artifacts during the visualization process (extrapolation and interpolation along a line).

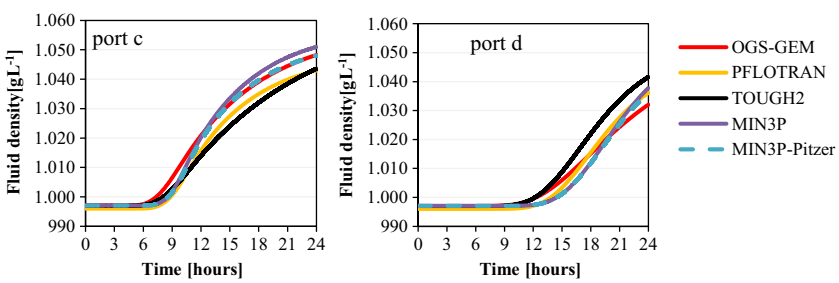

Fig. 9 Evolution of fluid density at ports "c" (left) and "d" (right) with time (case 2)

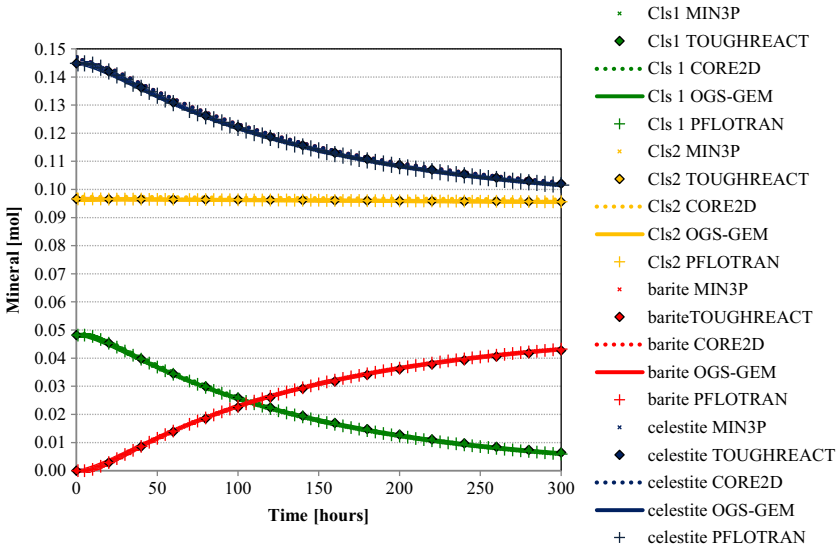

Fig. 10 Evolution of the bulk mineral composition in the flow cell with time (case 3a)

4.4 Case 3b

Case 3b is similar to case 3a but considers a stronger change in porosity due to mineral dissolution–precipitation. This was implemented as only small-grained $SrSO_4$ crystals were considered which results in a generally faster dissolution of celestite within the time window considered. After 200 h of $BaCl_2$ injection, about 60% of $SrSO_4$ was converted to $BaSO_4$, leading to localized clogging. Figure 13 compares the evolution of the bulk mineral composition with time in the flow cell as calculated by MIN3P-THCm, OpenGeoSys-GEM, PFLOTRAN, and TOUGHREACT. The results of all codes are in nearly perfect agreement.

Figure 14 compares the simulated concentrations of major aqueous species measured across line 1 at 100 h and 200 h. The results from the four codes are qualitatively in good agreement. As for case 3a, some discrepancies exist between the codes, which can be explained by the differences in the implementation of diffusive–dispersive transport.

The associated porosity and permeability decrease induced by the mineral transformation along line 1 is shown in Fig. 15. Calculated porosities and permeability profiles are not significantly different; for a given porosity of 0.013 after 200 h of reaction, the associated permeability is 1.3×10^{-18} m^2 for PFLOTRAN and OpenGeoSys-GEM and 1.11×10^{-18} for TOUGHREACT and MIN3P-THCm. Differences can be explained by the different formulations of the relationship between porosity and permeability implemented in MIN3P-THCm and TOUGHREACT compared to those used in OpenGeoSys-GEM and PFLOTRAN (Eqs. 10 and 11, respectively). These differences become more pronounced as porosity decreases with time. The results produced by MIN3P-THCm and TOUGHREACT were in perfect agreement. Although, OpenGeoSys-GEM and PFLOTRAN use the same equation-linking porosity and permeability, there are differences in the (spatial) calculated porosity and permeability of the two codes. This can be explained by the small differences observed in the ionic distribution (Fig. 14) and, consequently, mineral bulk transformations (Fig. 13) that influence the net porosity and, thus, permeability of the system. The differences in the spatial porosity and permeability calculated by the different codes have an impact on the evolution of temporal flow field with time and, consequently, on the observed small differences (after 100 h) in the total bulk mineral transformation inside the cell (Fig. 13).

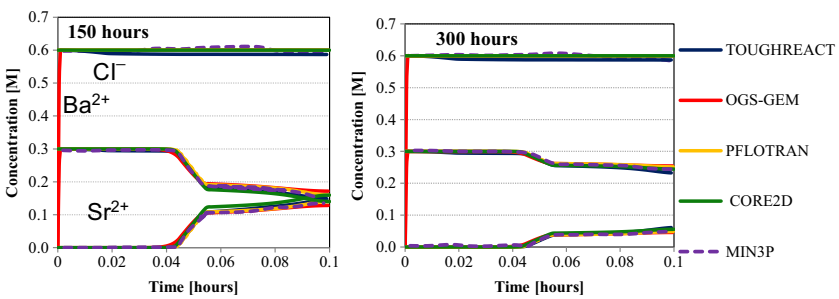

Fig. 11 Ionic concentrations measured across line 1 ($z = 0.01$ m) at 150 h and 300 h (case 3a)

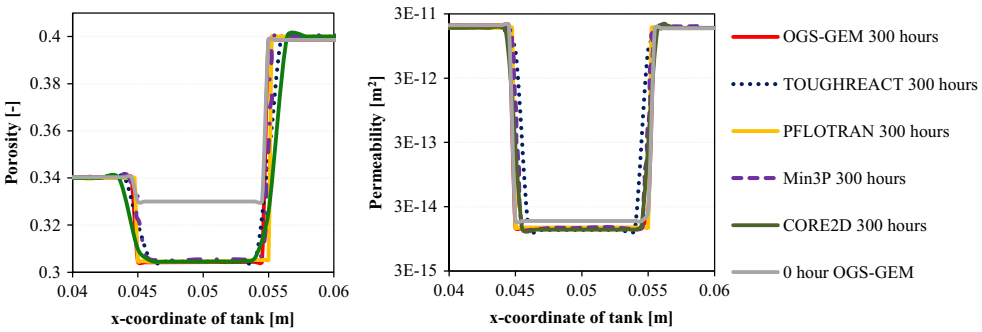

Fig. 12 Calculated porosity change (left) and permeability change (right) along line 1 (case 3a)

Besides other differences at the interfaces of the reactive media due to spatial discretization used by the codes as well as artifacts generated during the visualization process (extrapolation and interpolation), this also contributes to the observed differences in Fig. 15.

4.5 Case 4

In this case, the precipitation of a $SrSO_4$–$BaSO_4$ solid solution is considered instead of pure $BaSO_4$, which was the case for case 3. The injection of a solution which composed of 0.001 mol L^{-1} barium chloride and 0.099 mol L^{-1} strontium chloride is likely to produce a solid solution. When no Ba^{2+} is present, $SrSO_4$ exists as a pure celestite phase. When the concentration of Ba^{2+} exceeds the solubility of the solid solution, a solid solution having a greater stability compared to the pure barite phase (higher solubility compared to solid solution) will be formed preferentially. The transformation to a solid solution is kinetically controlled by the dissolution of the initial pure celestite phase.

Figure 16 shows the total amount of mineral phases present in the flow cell as a function of time. Although the time evolution of the system calculated by OpenGeoSys-GEM and TOUGHREACT is qualitatively in good agreement, there are differences in the composition of the solid solution calculated by each code. Usually, the thermodynamic description of solid solution should have a significant impact on the solubility of the solid phase and, therefore, on the chemical composition of the solid and aqueous phases. However, in this particular case, the concentrations of aqueous Ba in the Q2 and Q3 regions are close to zero and the discrepancies between the two codes are insignificant.

In GEM, the thermodynamic stability of a solid solution is increased by the consideration of the Gibbs energy of mixing (equal to the minus entropy of mixing times the temperature for an ideal solid solution; see Eq. 16). This term further decreases the solubility product of the solid solution compared to the pure end-member. Thus, minute amounts of barite present enhance the transformation of celestite to a more stable solid solution ($Sr_{1-x}Ba_xSO_4$) if no kinetic constraint for the formation of the solid solution is considered. On the other hand, for solid solutions, TOUGHREACT does not consider a pure equilibrium system where the backward–forward equilibration follows the Gibbs energy of mixing. Instead, it assumes that dissolution cannot re-equilibrate the entire solid grain precipitated from a solution. This is also the reason why TOUGHREACT cannot handle excess free energies of mixing and why it can only simulate ideal solid solutions. This difference in the conceptual approach yields a greater solubility of the solid solution and a lower amount of mineral transformation when compared to the GEM simulation (Fig. 16).

The porosity decrease and the corresponding permeability changes in this case study are insignificant and are therefore not presented.

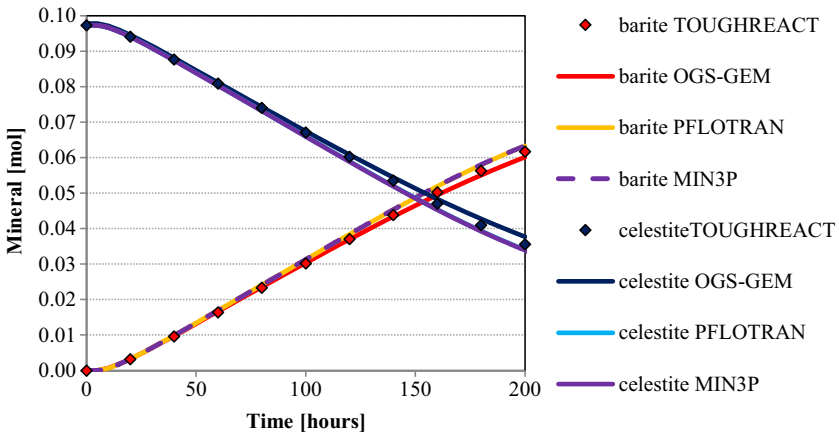

Fig. 13 Evolution of the bulk mineral composition in the flow cell with time (case 3b)

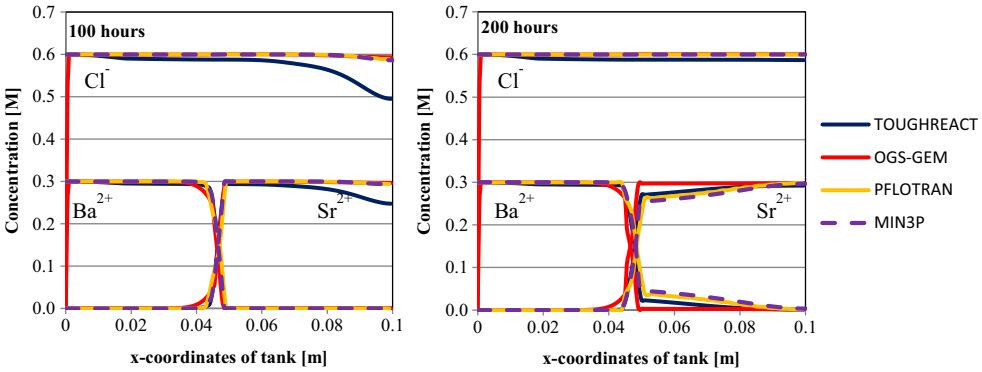

Fig. 14 Ionic concentrations [M] measured across line 1 ($z = 0.01$ m) at 100 h and 200 h (case 3b)

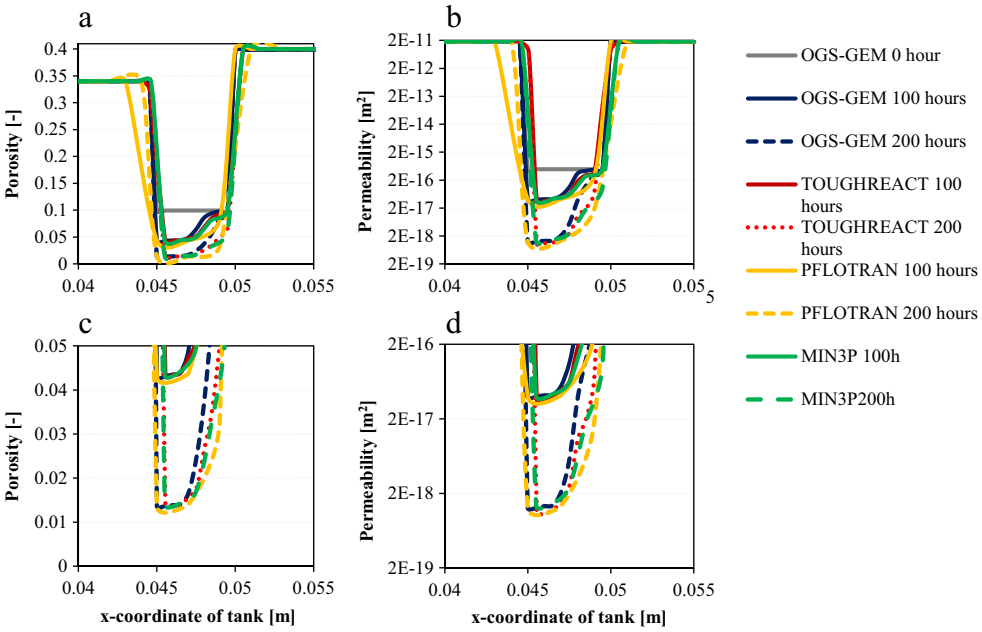

Fig. 15 Calculated **a** porosity change and **b** permeability change along line 1 (case 3b). **c**, **d** Partial diagram of **a** and **b**, respectively, with a narrower y-axis range to enable a better visualization of differences

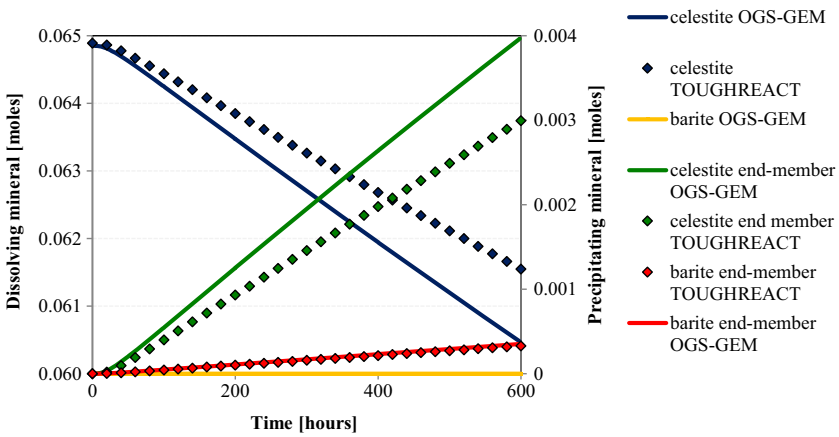

Fig. 16 Evolution of the bulk mineral composition in the flow cell with time. The left axis refers to the dissolving pure celestite while the right axis refers to the precipitating phases (end-members of the solid solution) (case 4)

5 Conclusions

We conducted 2D numerical experiments to benchmark fluid flow and reactive transport calculations. In the four presented benchmark cases, we studied several process combinations, such as the coupling of the flow with the conservative mass transport and the linking of the effect of liquid-phase density to the advective–diffusive transport of solutes. In addition, kinetically controlled dissolution–precipitation reactions causing porosity changes and new mineral formation were investigated. Codes involved in this benchmark initiative were CORE^{2D}, MIN3P-THCm, OpenGeoSys-GEM, PFLOTRAN, and TOUGHREACT. The results obtained in all the cases are in good qualitative agreement as long as the same material parameters and parameterizations are taken into account, e.g., the same reactive surfvace area model, the porosity update implementation, and the same porosity–permeability relationship. Differences in the implementation of the directional dispersion tensor as well as the intrinsic differences in the discretization schemes (finite element versus finite volume) explain most of the observed small differences, even in the most complex cases. Other difficulties in the comparison of the data, which can also generate artifacts, could be thought to arise from using data point grids of different densities. The investigated system behavior is robust against such small differences. In the case of the solid solution formation, the implemented conceptual models of solid solution simulation in different codes matter a lot, contributing to differences in the calculated solubility–controlled concentrations of dissolved species. In contrast, the predicted porosity evolution is not sensitive to the implemented solid solution approach.

The consistent results produced by the different codes do not imply; however, the constitutive equations (e.g., porosity–permeability, porosity–diffusivity, and reactive surface area models) implemented in the numerical codes are fully adequate. Experimental benchmarks have emphasized the further need of investigating these constitutive equations [27, 77, 78]. In addition, the reaction rates together with the numerical mesh discretization can also influence simulated porosity clogging scenarios [79]. Our numerical investigation implementing a simple chemical setup cannot be used directly for safety assessment of engineered barrier systems (nuclear waste repositories, geologic CO_2 storage, etc.). However, they provide an understanding of process coupling and a validation of underlying reactive transport concepts. A detailed understanding of process coupling within the dissolution–precipitation phenomena and feedback to transport properties is needed in order to do meaningful predictive modeling.

Acknowledgments We thank Dr. Dmitrii Kulik, Dr. Eric Sonnenthal, and Dr. Victor Vinograd for their useful discussion. We thank the comments, corrections, and suggestions of the two anonymous reviewers who contributed to the improvement of the paper.

Funding Information The first author gratefully acknowledges Nagra for funding her PhD thesis during most of the work presented in the manuscript was conducted. The contribution from the University of A Coruña was funded by the Spanish Ministry of Economy and Competitiveness (Grant number CGL2016-78281) with support from the FEDER funds. Jesús Fernández enjoyed a research contract from the FPI Program of the Spanish Ministry of Economy and Competitiveness.

Appendix A

Table 4 Equilibrium amount of solutes and phases (mol in 1 L of water) for boundary condition (BC) and initial condition (IC) for case 2

Case 2	Inlet (mol)	Q1 (mol)	Q2 (mol)	Q3 (mol)
Aqueous				
$Na(CO_3)^-$	$9.26E-010$	$8.72E-19$	$9.04E-19$	$8.72E-19$
$Na(HCO_3)(aq)$	$9.41E-007$	$1.38E-15$	$1.32E-15$	$1.38E-15$
$Na(SO_4)^-$	$4.74E-010$	$5.03E-18$	$2.42E-12$	$5.03E-18$
Na^+	1.3999991	$1.00E-09$	$9.98E-10$	$1.00E-09$
NaOH(aq)	$1.77E-009$	$2.69E-18$	$2.60E-18$	$2.69E-18$
$Sr(CO_3)(aq)$	$2.30E-018$	$2.99E-17$	$1.50E-11$	$2.99E-17$
$Sr(HCO_3)^+$	$5.82E-015$	$3.76E-14$	$1.94E-08$	$3.76E-14$
$Sr(SO_4)(aq)$	$1.33E-018$	$1.95E-16$	$4.54E-05$	$1.95E-16$
Sr^{2+}	$1.00E-009$	$1.00E-09$	$5.99E-04$	$1.00E-09$
$SrOH^+$	$3.13E-018$	$2.09E-17$	$1.09E-11$	$2.09E-17$
$CO_2(aq)$	$1.11E-005$	$1.36E-05$	$1.34E-05$	$1.36E-05$
CO_3^{-2}	$2.77E-010$	$4.67E-11$	$6.03E-11$	$4.67E-11$
HCO_3^-	$2.97E-006$	$2.45E-06$	$2.62E-06$	$2.45E-06$
Cl^-	1.4	$1.00E-09$	$1.00E-09$	$1.00E-09$
$H_2(aq)$	0	$0.00E+00$	$0.00E+00$	$0.00E+00$
Tracer(aq)	0.003	$1.00E-10$	$1.00E-10$	$1.00E-10$
$O_2(aq)$	0.00019	$2.30E-04$	$2.30E-04$	$2.30E-04$
HSO_4^-	$2.57E-014$	$2.39E-13$	$1.18E-07$	$2.39E-13$
SO_4^{-2}	$5.26E-010$	$1.00E-09$	$5.99E-04$	$1.00E-09$
OH^-	$4.75E-009$	$4.05E-09$	$4.39E-09$	$4.05E-09$
H^+	$3.92E-006$	$2.45E-06$	$2.52E-06$	$2.45E-06$
$H_2O(aq)$	$5.41E+01$	$5.53E+01$	$5.53E+01$	$5.53E+01$
Gaseous				
CO_2	0	$0.00E+00$	$0.00E+00$	$0.00E+00$
O_2	0	$0.00E+00$	$0.00E+00$	$0.00E+00$
Solid				
Quartz	$0.00E+00$	$8.55E+01$	$1.00E-09$	$6.47E+01$
$SrCO_3$	0	$0.00E+00$	$0.00E+00$	$0.00E+00$
$SrCl_2$	0	$0.00E+00$	$0.00E+00$	$0.00E+00$
$SrCl_2{\cdot}2H_2O$	0	$0.00E+00$	$0.00E+00$	$0.00E+00$
$SrCl_2{\cdot}6H_2O$	0	$0.00E+00$	$0.00E+00$	$0.00E+00$
$SrSO_4$	0	$0.00E+00$	$4.380E+01$	$0.00E+00$

Table 5 Equilibrium amount of solutes and phases (mol in 1 L of water) for boundary condition (BC) and initial condition (IC) for case 3a

Case 3a	Inlet (mol)	Q1_IC (mol)	Q2_IC (mol)	Q3_IC (mol)
Aqueous				
$Ba(CO_3)(aq)$	$6.44E-10$	$2.42E-17$	$1.69E-17$	$2.42E-17$
$Ba(HCO_3)^+$	$1.24E-06$	$2.35E-14$	$1.69E-14$	$2.35E-14$
$Ba(SO_4)(aq)$	$7.33E-10$	$5.02E-16$	$1.63E-10$	$5.02E-16$
Ba^{2+}	$3.00E-01$	$1.00E-09$	$8.37E-10$	$1.00E-09$
$BaOH^+$	$7.31E-10$	$1.38E-17$	$1.01E-17$	$1.38E-17$
$Sr(CO_3)(aq)$	$2.65E-18$	$2.99E-17$	$1.50E-11$	$2.99E-17$
$Sr(HCO_3)^+$	$6.60E-15$	$3.76E-14$	$1.94E-08$	$3.76E-14$
$Sr(SO_4)(aq)$	$9.51E-19$	$1.95E-16$	$4.54E-05$	$1.95E-16$
Sr^{2+}	$1.00E-09$	$1.00E-09$	$5.99E-04$	$1.00E-09$
$SrOH^+$	$3.69E-18$	$2.09E-17$	$1.09E-11$	$2.09E-17$
$CO_2(aq)$	$1.17E-05$	$1.35E-05$	$1.34E-05$	$1.35E-05$
CO_3^{-2}	$2.28E-10$	$4.67E-11$	$6.04E-11$	$4.67E-11$
HCO_3^-	$2.97E-06$	$2.45E-06$	$2.62E-06$	$2.45E-06$
Cl^-	$6.00E-01$	$2.00E-09$	$2.00E-09$	$2.00E-09$
$H_2(aq)$	$0.00E+00$	$0.00E+00$	$0.00E+00$	$0.00E+00$
$O_2(aq)$	$2.00E-04$	$2.30E-04$	$2.30E-04$	$2.30E-04$
HSO_4^-	$1.59E-14$	$2.39E-13$	$1.18E-07$	$2.39E-13$
SO_4^{-2}	$2.67E-10$	$1.00E-09$	$5.99E-04$	$1.00E-09$
OH^-	$4.95E-09$	$4.06E-09$	$4.39E-09$	$4.06E-09$
H^+	$4.22E-06$	$2.45E-06$	$2.52E-06$	$2.45E-06$
$H_2O(aq)$	$5.50E+01$	$5.54E+01$	$5.53E+01$	$5.54E+01$
Gaseous				
CO_2	$0.00E+00$	$0.00E+00$	$0.00E+00$	$0.00E+00$
H_2	$0.00E+00$	$0.00E+00$	$0.00E+00$	$0.00E+00$
O_2	$0.00E+00$	$0.00E+00$	$0.00E+00$	$0.00E+00$
Solid				
$BaCO_3$	$0.00E+00$	$0.00E+00$	$0.00E+00$	$0.00E+00$
$BaCl_2$	$0.00E+00$	$0.00E+00$	$0.00E+00$	$0.00E+00$
$BaCl_2{\cdot}2H_2O$	$0.00E+00$	$0.00E+00$	$0.00E+00$	$0.00E+00$
$BaCl_2{\cdot}H_2O$	$0.00E+00$	$0.00E+00$	$0.00E+00$	$0.00E+00$
$BaSO_4$	$0.00E+00$	$0.00E+00$	$0.00E+00$	$0.00E+00$
Quartz	$0.00E+00$	$8.551E+01$	$1.00E-09$	$6.657E+01$
$SrCO_3$	$0.00E+00$	$0.00E+00$	$0.00E+00$	$0.00E+00$
$SrCl_2$	$0.00E+00$	$0.00E+00$	$0.00E+00$	$0.00E+00$
$SrCl_2{\cdot}2H_2O$	$0.00E+00$	$0.00E+00$	$0.00E+00$	$0.00E+00$
$SrCl_2{\cdot}6H_2O$	$0.00E+00$	$0.00E+00$	$0.00E+00$	$0.00E+00$
$SrSO_4$ (Cls 1)	$0.00E+00$	$0.00E+00$	$1.466E+01$	$0.00E+00$
$SrSO_4$ (Cls 2)	$0.00E+00$	$0.00E+00$	$2.931E+01$	$0.00E+00$

Table 6 Equilibrium amount of solutes and phases (mol in 1 L of water) for boundary condition (BC) and initial condition (IC) for case 3b

Case 3b	Inlet (mol)	Q1_IC (mol)	Q2_IC (mol)	Q3_IC (mol)
Aqueous				
$Ba(CO_3)(aq)$	$6.44E-10$	$2.42E-17$	$8.35E-17$	$2.42E-17$
$Ba(HCO_3)^+$	$1.24E-06$	$2.35E-14$	$8.35E-14$	$2.35E-14$
$Ba(SO_4)(aq)$	$7.33E-10$	$5.02E-16$	$8.93E-10$	$5.02E-16$
Ba^{2+}	$3.00E-01$	$1.00E-09$	$3.91E-09$	$1.00E-09$
$BaOH^+$	$7.31E-10$	$1.38E-17$	$4.95E-17$	$1.38E-17$
$Sr(CO_3)(aq)$	$2.65E-18$	$2.99E-17$	$1.53E-11$	$2.99E-17$
$Sr(HCO_3)^+$	$6.60E-15$	$3.76E-14$	$1.97E-08$	$3.76E-14$
$Sr(SO_4)(aq)$	$9.51E-19$	$1.95E-16$	$4.56E-05$	$1.95E-16$
Sr^{2+}	$1.00E-09$	$1.00E-09$	$5.90E-4$	$1.00E-09$
$SrOH^+$	$3.69E-18$	$2.09E-17$	$1.11E-11$	$2.09E-17$
$CO_2(aq)$	$1.17E-05$	$1.35E-05$	$1.33E-05$	$1.35E-05$
CO_3^{-2}	$2.28E-10$	$4.67E-11$	$6.13E-11$	$4.67E-11$
HCO_3^-	$2.97E-06$	$2.45E-06$	$2.64E-06$	$2.45E-06$
Cl^-	$6.00E-01$	$2.00E-09$	$9.60E-09$	$2.00E-09$
$H_2(aq)$	$0.00E+00$	$0.00E+00$	0	$0.00E+00$
$O_2(aq)$	$2.00E-04$	$2.30E-04$	0.00023	$2.30E-04$
HSO_4^-	$1.59E-14$	$2.39E-13$	$1.20E-07$	$2.39E-13$
SO_4^{-2}	$2.67E-10$	$1.00E-09$	0.000590257	$1.00E-09$
OH^-	$4.95E-09$	$4.06E-09$	$4.48E-09$	$4.06E-09$
H^+	$4.22E-06$	$2.45E-06$	$2.54E-06$	$2.45E-06$
$H_2O(aq)$	$5.50E+01$	$5.54E+01$	55.397354	$5.54E+01$
Gaseous				
CO_2	$0.00E+00$	$0.00E+00$	0	$0.00E+00$
H_2	$0.00E+00$	$0.00E+00$	0	$0.00E+00$
O_2	$0.00E+00$	$0.00E+00$	0	$0.00E+00$
Solid				
$BaCO_3$	$0.00E+00$	$0.00E+00$	0	$0.00E+00$
$BaCl_2$	$0.00E+00$	$0.00E+00$	0	$0.00E+00$
$BaCl_2{\cdot}2H_2O$	$0.00E+00$	$0.00E+00$	0	$0.00E+00$
$BaCl_2{\cdot}H_2O$	$0.00E+00$	$0.00E+00$	0	$0.00E+00$
$BaSO_4$	$0.00E+00$	$0.00E+00$	0	$0.00E+00$
Quartz	$0.00E+00$	$8.551E+01$	$1.00E-06$	$6.657E+01$
$SrCO_3$	$0.00E+00$	$0.00E+00$	0	$0.00E+00$
$SrCl_2$	$0.00E+00$	$0.00E+00$	0	$0.00E+00$
$SrCl_2{\cdot}2H_2O$	$0.00E+00$	$0.00E+00$	0	$0.00E+00$
$SrCl_2{\cdot}6H_2O$	$0.00E+00$	$0.00E+00$	0	$0.00E+00$
$SrSO_4$Cls 2	$0.00E+00$	$0.00E+00$	194.5704	$0.00E+00$

Table 7 Equilibrium amount of solutes and phases (mol in 1L of water) for boundary(BC) and initial conditions (IC) for case 4

Case 4	Inlet (mol)	Q1_IC (mol)	Q2_IC (mol)	Q3_IC (mol)
Aqueous				
$Ba(CO_3)(aq)$	$2.98E{-}12$	$1.62E{-}17$	$3.43E{-}18$	$1.63E{-}17$
$Ba(HCO_3)^+$	$5.52E{-}09$	$1.96E{-}14$	$4.20E{-}15$	$1.97E{-}14$
$Ba(SO_4)(aq)$	$1.23E{-}11$	$5.02E{-}16$	$4.78E{-}11$	$5.02E{-}16$
Ba^{2+}	$1.00E{-}03$	$1.00E{-}09$	$2.46E{-}10$	$1.00E{-}09$
$BaOH^+$	$3.33E{-}12$	$1.11E{-}17$	$2.41E{-}18$	$1.11E{-}17$
$Sr(CO_3)(aq)$	$3.65E{-}10$	$2.01E{-}17$	$1.03E{-}11$	$2.01E{-}17$
$Sr(HCO_3)^+$	$8.72E{-}07$	$3.13E{-}14$	$1.63E{-}08$	$3.15E{-}14$
$Sr(SO_4)(aq)$	$4.73E{-}10$	$1.95E{-}16$	$4.54E{-}05$	$1.95E{-}16$
Sr^{2+}	$9.90E{-}02$	$1.00E{-}09$	$5.99E{-}04$	$1.00E{-}09$
$SrOH^+$	$4.99E{-}10$	$1.68E{-}17$	$8.91E{-}12$	$1.67E{-}17$
$CO_2(aq)$	$1.25E{-}05$	$1.40E{-}05$	$1.38E{-}05$	$1.41E{-}05$
CO_3^{-2}	$1.21E{-}10$	$3.13E{-}11$	$4.17E{-}11$	$3.14E{-}11$
HCO_3^-	$2.57E{-}06$	$2.04E{-}06$	$2.21E{-}06$	$2.05E{-}06$
Cl^-	$2.00E{-}01$	$1.00E{-}06$	$1.00E{-}06$	$1.00E{-}06$
$H_2(aq)$	$0.00E{+}00$	$0.00E{+}00$	$0.00E{+}00$	$0.00E{+}00$
$O_2(aq)$	$2.52E{-}04$	$2.52E{-}04$	$2.50E{-}04$	$2.50E{-}04$
HSO_4^-	$5.00E{-}14$	$2.96E{-}13$	$1.45E{-}07$	$2.98E{-}13$
SO_4^{-2}	$5.15E{-}10$	$1.00E{-}09$	$5.99E{-}04$	$1.00E{-}09$
OH^-	$4.40E{-}09$	$3.27E{-}09$	$3.59E{-}09$	$3.25E{-}09$
H^+	$4.46E{-}06$	$3.04E{-}06$	$3.08E{-}06$	$3.06E{-}06$
$H_2O(aq)$	$5.53E{+}01$	$5.53E{+}01$	$5.53E{+}01$	$5.53E{+}01$
Gaseous				
CO_2	$0.00E{+}00$	$0.00E{+}00$	$0.00E{+}00$	$0.00E{+}00$
H_2	$0.00E{+}00$	$0.00E{+}00$	$0.00E{+}00$	$0.00E{+}00$
O_2	$0.00E{+}00$	$0.00E{+}00$	$0.00E{+}00$	$0.00E{+}00$
Solid				
$BaSO_4$	$0.00E{+}00$	$0.00E{+}00$	$7.07E{-}10$	$0.00E{+}00$
end−member				
$SrSO_4$	$0.00E{+}00$	$0.00E{+}00$	$3.64E{-}06$	$0.00E{+}00$
end−member				
$BaCO_3$	$0.00E{+}00$	$0.00E{+}00$	$0.00E{+}00$	$0.00E{+}00$
$BaCl_2$	$0.00E{+}00$	$0.00E{+}00$	$0.00E{+}00$	$0.00E{+}00$
$BaCl_2 \cdot 2H_2O$	$0.00E{+}00$	$0.00E{+}00$	$0.00E{+}00$	$0.00E{+}00$
$BaCl_2 \cdot H_2O$	$0.00E{+}00$	$0.00E{+}00$	$0.00E{+}00$	$0.00E{+}00$
$BaSO_4$	$0.00E{+}00$	$0.00E{+}00$	$0.00E{+}00$	$0.00E{+}00$
Quartz	$0.00E{+}00$	$8.55E{+}01$	$1.00E{-}09$	$6.62E{+}01$
$SrCO_3$	$0.00E{+}00$	$0.00E{+}00$	$0.00E{+}00$	$0.00E{+}00$
$SrCl_2$	$0.00E{+}00$	$0.00E{+}00$	$0.00E{+}00$	$0.00E{+}00$
$SrCl_2 \cdot 2H_2O$	$0.00E{+}00$	$0.00E{+}00$	$0.00E{+}00$	$0.00E{+}00$
$SrCl_2 \cdot 6H_2O$	$0.00E{+}00$	$0.00E{+}00$	$0.00E{+}00$	$0.00E{+}00$
$SrSO_4$	$0.00E{+}00$	$0.00E{+}00$	$3.24E{+}01$	$0.00E{+}00$

Appendix B: Solid solution

Activities of the end-members of a solid solution in thermodynamic equilibrium are related to activities of aqueous ions by the following set of equations [80]:

$$SO_4^{2-} = a_{SrSO_4} K^0_{SrSO_4} = \gamma_{SrSO_4} X_{SrSO_4} K^0_{SrSO_4} \quad (22)$$

$$SO_4^{2-} = a_{BaSO_4} K^0_{BaSO_4} = \gamma_{BaSO_4} X_{BaSO_4} K^0_{BaSO_4} \quad (23)$$

where a_i, γ_i, and X_i are the activity, the activity coefficient, and the mole fraction of an end-member i, respectively. For a simple ideal solid solution, γ_i is equal to 1, such that the activity of an end-member is equal to its mole fraction

$$a_{BaSO_4} = X_{BaSO_4} \quad (24)$$

$$a_{SrSO_4} = X_{SrSO_4} \quad (25)$$

The solidus and solutus curves are derived from the following formula:

$$\log \sum \prod (\text{solidus}) = \log \left(a_{SrSO_4} K^0_{SrSO_4} + a_{BaSO_4} K^0_{BaSO_4} \right) \quad (26)$$

$$\log \sum \prod (\text{solutus}) = \log \left(\frac{1}{x_{Ba^{2+}} \Big/ K^0_{BaSO_4} + x_{Sr^{2+}} \Big/ K^0_{SrSO_4}} \right) \quad (27)$$

The solidus x-scale refers to the mole fraction of the end-members while the solutus x-scale is calculated as

$$x_{Ba^{2+}} = \frac{a_{BaSO_4} K^0_{BaSO_4}}{\sum \prod (\text{solidus})} \quad (28)$$

$$x_{Sr^{2+}} = 1 - x_{Ba^{2+}} \quad (29)$$

N.B.: in this section only (Appendix B), a refers to the activity different from a used in the manuscript which refers to surface area per volume of the mineral phase.

References

1. Alt-Epping, P., Diamond, L.W., Häring, M.O., Ladner, F., Meier, D.B.: Prediction of water-rock interaction and porosity evolution in a granitoid-hosted enhanced geothermal system, using constraints from the 5 km Basel-1 well. Appl. Geochem. **38**, 121–133 (2013)
2. Alt-Epping, P., Waber, H.N., Diamond, L.W., Eichinger, L.: Reactive transport modeling of the geothermal system at Bad Blumau, Austria: implications of the combined extraction of heat and CO_2. Geothermics **45**, 18–30 (2013)
3. Wanner, C., Peiffer, L., Sonnenthal, E.L., Spycher, N., Iovenitti, J., Kennedy, B.M.: Reactive transport modeling of the Dixie Valley geothermal area: insights on flow and geothermometry. Geothermics **51**, 130–141 (2014)
4. Diamond, L.W., Alt-epping, P.: Predictive modelling of mineral scaling, corrosion and the performance of solute geothermometers in a granitoid-hosted, enhanced geothermal system. Appl. Geochem. **51**, 216–228 (2014)
5. De Windt, L., Pellegrini, D., van der Lee, J.: Coupled modeling of cement/claystone interactions and radionuclide migration. J. Contam. Hydrol. **68**(3-4), 165–182 (2004)
6. Gaucher, E.C., Blanc, P.: Cement/clay interaction—a review: experiments, natural analogues, and modelling. Waste Manag. **26**(7), 776–788 (2006)

7. De Windt, L., Badredinne, R., Lagneau, V.: Long-term reactive transport modelling of stabilized/solidified waste: from dynamic leaching tests to disposal scenarios. J. Hazard. Mater. **139**(3), 529–536 (2007)
8. Kosakowski, G., Berner, U.: The evolution of clay rock/cement interfaces in a cementitious repository for low and intermediate level radioactive waste. Phys. Chem. Earth A/B/C **64**, 65–86 (2013)
9. Berner, U., Kulik, D.A., Kosakowski, G.: Geochemical impact of a low-pH cement liner on the near field of a repository for spent fuel and high-level radioactive waste. Phys. Chem. Earth **46-56**, 64 (2013)
10. Gaus, I., Azaroual, M., Czernichowski-Lauriol, I.: Reactive transport modelling of the impact of CO_2 injection on the clayey cap rock at Sleipner (North Sea). Chem. Geol. **217**(3-4), 319–337 (2005)
11. Class, H., Ebigbo, A., Helmig, R., Dahle, H.K., Nordbotten, J.M., Celia, M.A., Aubigane, P., Darcis, M., Ennis-King, J., Fan, Y., Flemisch, B., Gasda, S.E., Jin, M., Krug, S., Labregere, D., Beni, A.N., Pawar, R.J., Sbai, A., Thomas, S.G., Trenty, L., Wei, L.: A benchmark study problems related to CO_2 storage in geologic formations. Computat. Geosci. **13**(4), 409–434 (2009)
12. Bildstein, O., Kervévan, C., Lagneau, V., Delaplace, P., Crédoz, A., Audigane, P., Perfetti, E., Jacquemet, N., Jullien, M.: Integrative modeling of caprock integrity in the context of CO_2 storage: evolution of transport and geochemical properties and impact on performance and safety assessment. Oil Gas Sci. Technol. IFP **65**(3), 485–502 (2010)
13. Wanner, C., Eggenberger, U., Mäder, U.: A chromate-contaminated site in southern Switzerland—part 2: reactive transport modeling to optimize remediation options. Appl. Geochem. **27**(3), 655–662 (2012)
14. Jamieson-Hanes, J.H., Amos, R.T., Blowes, D.W.: Reactive transport modeling of chromium isotope fractionation during cr(IV) reduction. Environ. Sci. Technol. **46**(24), 13311–13316 (2012)
15. Wanner, C., Sonnenthal, E.L.: Assessing the control on the effective kinetic Cr isotope fractionation factor: a reactive transport modeling approach. Chem. Geol. **337-338**, 88–98 (2013)
16. Lagneau, V., van der Lee, J.: Operator-splitting-based reactive transport models in strong feedback of porosity change: the contribution of analytical solutions for accuracy validation and estimator improvement. J. Contam. Hydrol. **112**(1-4), 118–129 (2010)
17. Hayek, M., Kosakowski, G., Churakov, S.: Exact analytical solutions for a diffusion problem coupled with a precipitation-dissolution reaction and feedback of porosity change. Water Resour Res. **47**, W07545 (2011)
18. Hayek, M., Kosakowski, G., Jakob, A., Churakov, S.V.: A class of analytical solutions for multidimensional multispecies diffusive transport coupled with precipitation-dissolution reactions and porosity changes. Water Resour. Res. **48**, W03525 (2012)
19. van der Lee, J., De Windt, L., Lagneau, V., Goblet, P.: Module oriented modeling of reactive transport with HYTEC. Comput. Geosci. **29**(3), 265–275 (2003)
20. Lagneau, V.: Influence Des Processus Géochimiques Sur Le Transport En Milieu Poreux: Application Au Colmatage De BarriéRes De Confinement Potentielles Dans Un Stockage En Formation GéOlogique. PhD Thesis, Ecole des Mines de Paris (2000)
21. Tartakovsky, A.M., Redden, G., Lichtner, P.C., Scheibe, T.D., Meakin, P.: Mixing-induced precipitation: experimental study and multiscale numerical analysis. Water Resour. Res. **44**, W06S04 (2008)
22. Katz, G.E., Berkowitz, B., Guadagnini, A., Saaltink, M.W.: Experimental and modeling investigation of multicomponent reactive transport in porous media. J. Contam. Hydrol. **120-121**, 27–44 (2011)
23. Steefel, C.I., Appelo, C.A.J., Arora, B., Jacques, D., Kalbacher, T., Kolditz, O., Lagneau, V., Lichtner, P.C., Mayer, K.U., Meeussen, J.C.L., Molins, S., Moulton, D., Shao, H., Šimůnek, J., Spycher, N.F., Yabusaki, S.B., Yeh, G.T.: Reactive transport codes for subsurface environmental simulation. Computat. Geosci. **19**, 445–478 (2015)
24. Steefel, C.I., Yabusaki, S.B., Mayer, K.U.: Reactive transport benchmarks for subsurface environmental simulation. Computat. Geosci. **19**, 439–443 (2015)
25. Xie, M., Mayer, K.U., Claret, F., Alt-Epping, P., Jacques, D., Steefel, C., Chiaberge, C., Šimůnek, J.: Implementation and evaluation of permeability-porosity and tortuosity-porosity relationships linked to mineral dissolution-precipitation. Computat. Geosci. **19**, 655–671 (2015)
26. Cochepin, B., Trotignon, L., Bildstein, O., Steefel, C.I., Lagneau, V., van der Lee, J.: Approaches to modelling coupled flow and reaction in a 2D cementation experiment. Adv. Water Resour. **31**(12), 1540–1551 (2008)
27. Poonoosamy, J., Kosakowski, G., Van Loon, L.R., Mäder, U.: Dissolution-precipitation processes in tank experiments for testing numerical models for reactive transport calculations: experiment and modelling. J. Contam. Hydrol. **177-178**, 1–17 (2015)
28. Poonoosamy, J., Curti, E., Kosakowski, G., Grolimund, D., Van Loon, L.R., Mäder, U.: Barite precipitation following celestite dissolution in a porous medium: a SEM/BSE and μ-XRD/XRF study. Geochim. Cosmochim. Acta **182**, 131–144 (2016)
29. Prasianakis, N.I., Curti, E., Kosakowski, G., Poonoosamy, J., Churakov, S.V.: Deciphering pore-level precipitation mechanisms. Sci. Rep. **7**, 13765 (2017)
30. Samper, J., Xu, T., Yang, C.: A sequential partly iterative approach for multicomponent reactive transport with $CORE^{2D}$. Computat. Geosci. **13**, 301–316 (2009)
31. Samper, J., Yang, C., Zheng, L., Montenegro, L., Xu, T., Dai, Z., Zhang, G., Lu, C., Moreira, S.: $CORE^{2D}$ V4: a code for water flow, heat and solute transport, geochemical reactions, and microbial processes. In: Zhang F., Yeh G.T, Parker C., Shi X. (eds.) Chapter 7 of the Electronic Book Groundwater Reactive Transport Models, pp. 161–186. Bentham Science, ISBN 978-1-60805-029-1 (2011)
32. Samper, J., Lu, C., Montenegro, L.: Reactive transport model of interactions of corrosion products and bentonite. Phys. Chem. Earth **33**, S306–S316 (2008)
33. Yang, C., Samper, J., Molinero, J.: Inverse microbial and geochemical reactive transport models in porous media. Phys. Chem. Earth **33**(12-13), 1026–1034 (2008)
34. Zheng, L., Samper, J.: Coupled THMC model of FEBEX mock-up test. Phys. Chem. Earth **33**, 486–498 (2008)
35. Zheng, L., Samper, J., Montenegro, L., Fernández, A.M.: A coupled THMC model of a heating and hydration laboratory experiment in unsaturated compacted FEBEX bentonite. J. Hydrol. **386**, 80–94 (2010)
36. Zheng, L., Samper, J., Montenegro, L.: A coupled THC model of the FEBEX in situ test with bentonite swelling and chemical and thermal osmosis. J. Contam. Hydrol. **126**, 45–60 (2011)
37. Samper, J., Mon, A., Montenegro, L.: A revisited thermal, hydrodynamic, chemical and mechanical model of compacted bentonite for the entire duration of the FEBEX in situ test. Applied Clay Sciences, https://doi.org/10.1016/j.clay.2018.02.019 (2018)
38. Samper, J., Zheng, L., Montenegro, L., Fernández, A.M., Rivas, P.: Coupled thermo-hydro-chemical models of compacted bentonite after FEBEX in situ test. Appl. Geochem. **23**(5), 1186–1201 (2008)
39. Samper, J., Naves, A., Montenegro, L., Mon, A.: Reactive transport modelling of the long-term interactions of corrosion

products and compacted bentonite in a HLW repository in granite: uncertainties and relevance for performance assessment. Appl. Geochem. **67**, 42–51 (2016)
40. Mon, A., Samper, J., Montenegro, L., Naves, A., Fernández, J.: Long-term nonisothermal reactive transport model of compacted bentonite, concrete and corrosion products in a HLW repository in clay. J Cont. Hydrol. **197**, 1–16 (2017)
41. Mayer, K.U., Frind, E.O., Blowes, D.W.: Multicomponent reactive transport modeling in variably saturated porous media using a generalized formulation for kinetically controlled reactions. Water Resour. Res. **38**(9), 1174 (2002). https://doi.org/10.1029/2001WR000862
42. Kulik, D.A., Wagner, T., Dmytrieva, S.V., Kosakowski, G., Hingerl, F.F., Chudnenko, K.V., Berner, U.: GEM-Selektor geochemical modeling package: revised algorithm and GEMS3k numerical kernel for coupled simulation codes. Computat. Geosci. **17**(1), 1–24 (2013)
43. Shao, H., Dmytrieva, S.V., Kolditz, O., Kulik, D.A., Pfingsten, W., Kosakowski, G.: Modeling reactive transport in non-ideal aqueous–solid solution system. Appl. Geochem. **24**(7), 1287–1300 (2009)
44. Kosakowski, G., Watanabe, N.: Opengeosys-gem: a numerical tool for calculating geochemical and porosity changes in saturated and partially saturated media. Phys. Chem. Earth **70-71**, 138–149 (2014)
45. Wagner, T., Kulik, D.A., Hingerl, F.F., Dmytrieva, S.V.: GEM-Selektor geochemical modeling package: TSolMod C++ class library and data interface for multicomponent phase models. Can. Mineral. **50**, 1173–1195 (2012)
46. Lichtner, P.C., Hammond, G.E., Lu, C., Karra, S., Bisht, G., Andre, B., Mills, R.T., Kumar, J., Frederick, J.M.: PFLOTRAN user manual, release 1.1, http://www.documentation.pflotran.org (2017)
47. Xu, T., Spycher, N., Sonnenthal, E., Zhang, G., Zheng, L., Pruess, K.: TOUGHREACT Version 2.0: a simulator for subsurface reactive transport under non-isothermal multiphase flow conditions. Comput. Geosci. **37**(6), 763–774 (2011)
48. Pruess, K., Oldenburg, C.M., Moridis, G.: TOUGH2 User's Guide, Version 2.0. Lawrence Berkeley National Laboratory Report LBNL-29400, Berkeley, California (1999)
49. Batzle, M., Wang, Z.: Seismic properties of pore fluids. Geophysics **57**(11), 1396–1408 (1992)
50. Henderson, R.D., Day-Lewis, F.D., Abarca, E., Harvey, C.F., Karam, H.N., Liu, L., Lane, J.W. Jr.: Marine electrical resistivity imaging of submarine groundwater discharge: sensitivity analysis and application in Waquoit Bay, Massachusetts, USA. Hydrogeol. J. **18**, 173–185 (2010)
51. Frind, E.O.: Simulation of long term transient density dependent transport in groundwater. Adv. Water Resour. **5**, 73–98 (1982)
52. Voss, C.I.: SUTRA—A Finite-element Simulation Model for Saturated-unsaturated, Fluid-density-dependent Ground-water Flow with Energy Transport or Chemically-reactive Single-species Solute Transport, vol. 409. U.S. Geological Survey Water-Resources Investigations Report 84–4369 (1984)
53. Kharaka, Y., Gunter, W., Aggarwal, P., Perkins, E., Debraal, J.: SOLMINEQ. 88: A Computer Program for Geochemical Modeling of Water-rock Interactions U.S. Geol. Surv. Water Resour. Invest. Rep. 88–4227 (1988)
54. Guo, W., Langevin, C.: User's Guide to SEAWAT: A Computer Program for Simulation of Three-dimensional Variable Density Ground-water Flow. U.S. Geologigical Survey Water-Resources Investigations Report 88–4227. https://pubs.usgs.gov/wri/1988/4227/report.pdf (1988) (2002)
55. Simpson, M.J., Clement, T.P.: Improving the worthiness of the Henry problem as a benchmark for density-dependent groundwater flow models. Water Resour. Res. **40**, W01504 (2004). https://doi.org/10.1029/2003WR002199
56. Kemp, N.P., Thomas, D.C., Atkinson, G., Atkinson, B.L.: Density modeling for brines as a function of composition, temperature and pressure. SPE Prod. Eng. **4**, 394–400 (1989)
57. Monnin, C.: Density calculation and concentration scale conversions for natural waters. Comput. Geosci. **20**(10), 1435-1445 (1994)
58. Bea, S.A., Carrera, J., Ayora, C., Batlle, F.: Pitzer algorithm: efficient implementation of Pitzer equations in geochemical and reactive transport models. Comput. Geosci. **36**, 526–538 (2012)
59. Bea, S.A., Mayer, K.U., MacQuarrie, K.T.B.: Modelling Reactive Transport in Sedimentary Rock Environments—Phase II, MIN3P-THCm code enhancements and illustrative simulations for a glaciation scenario Technical report: NWMO TR-2011-13 (2011)
60. Archie, G.: The electrical resistivity log as an aid in determining some reservoir characteristics. Trans. AIME **146**, 54–62 (1942)
61. Bear, J.: Dynamics of Fluids in Porous Media. Dover Publications Inc., New York (1972)
62. Helgeson, H.C., Kirkham, D.H., Flowers, G.C.: Theoretical prediction of the thermodynamic behavior of aqueous electrolytes at high pressures and temperatures: IV. Calculation of activity coefficients, osmotic coefficients, and apparent molal and standard and relative partial molal properties to 600 °C and 5 KB. Am. J. Sci. **281**, 1249–1516 (1981)
63. Johnson, J.W., Oelkers, E.H., Helgeson, H.C.: SUPCRT92: A software package for calculating the standard molal thermodynamic properties of minerals, gases, aqueous species, and reactions from 1 to 5000 bar and 0 to 1000 °C. Computat. Geosci. **18**(7), 899–947 (1992)
64. Pitzer, K.S.: Thermodynamics of electrolytes. I. Theoretical basis and general equations. J. Phys. Chem. **77**, 268-277 (1973)
65. Pitzer, K.S.: Ion interaction approach: theory and data correlation. In: Pitzer, K.S. (ed.) Activity Coefficients in Electrolyte Solutions. CRC, Boca Raton (1991)
66. Palandri, J.L., Kharaka, Y.K.: A Compilation of Rate Parameters of Water Mineral Interaction Kinetics for Application to Geochemical Modelling. US Geological Survey, Menlo Park (2004)
67. Dove, P.M., Czank, C.A.: Crystal chemical controls on the dissolution kinetics of the isostructural sulfates: celestite, anglesite, and barite. Geochim. Cosmochim. Acta **56**(10), 4147–4156 (1995)
68. Bruno, J., Bosbach, D., Kulik, D., Navrotsky, A.: Chemical Thermodynamics of Solid Solutions of Interest in Radioactive Waste Management: a State-Of-The Art Report Chemical Thermodynamics. In: Mompean, F.J., Illemassene, M., Perrone, J. (eds.) OECD, vol. 10. Issy-les-Moulineaux (2007)
69. Wanner, C., Druhan, J.L., Amos, R.T., Alt-Epping, P., Steefel, C.I.: Benchmarking the simulation of Cr isotope fractionation. Computat. Geosci. **19**, 497–521 (2015)
70. Hummel, W., Berner, U., Curti, E., Pearson, F.J., Thoenen, T.: Nagra/PSI Chemical Thermodynamic Data Base 01/01. Universal, Parkland (2002)
71. Shock, E.L., Helgeson, H.C., Sverjensky, D.A.: Calculation of the thermodynamic and properties of aqueous species at high pressures temperatures: standard partial molal properties inorganic neutral species. Geochim. Cosmochim. Acta **53**(9), 2157–2183 (1989)
72. Sverjensky, D.A., Shock, E.L., Helgeson, H.C.: Prediction of the thermodynamic properties of aqueous metal complexes to 1000 °C and 5 kb. Geochim. Cosmochim. Acta **61**, 1359–1412 (1997)
73. Shock, E., Sassani, D.C., Willis, M., Sverjensky, D.A.: Inorganic species in geologic fluids: correlations among standard molal

thermodynamic properties of aqueous ions and hydroxide complexes. Geochim. Cosmochim. Acta **61**(5), 907–950 (1997)
74. Wagman, D.D., Evans, W.H., Parker, V.B., Schumm, R.H., Halow, I., Bailey, S.M., Churney, K.L., Nuttall, R.L.: The NBS tables of chemical and thermodynamic properties. Selected values for inorganic and C1 and C2 organic substances in SI units. J. Phys. Chem. Ref. Data **11**(2), 392 (1982)
75. Kelley, K.K.: Contributions to the Data in Theoretical Metallurgy XIII: High Temperature Heat Content, Heat Capacities and Entropy Data for the Elements and Inorganic Compounds. U.S. Bureau of Mines Bulletin 584, USA (1960)
76. Helgeson, H.C., Delany, J., Nesbitt, H.W., Bird, D.K.: Summary and critique of the thermodynamic properties of rock-forming minerals. Am. J. Sci. **278A**, 229 (1978)
77. Chagneau, A., Claret, F., Enzmann, F., Kersten, M., Heck, S., Madé, B., Schäfer, T.: Mineral precipitation-induced porosity reduction and its effect on transport parameters in diffusion-controlled porous media. Geochem. Trans. **16**, 13 (2015)
78. Noiriel, C., Luquot, L., Madé, B., Raimbault, L., Gouze, P., Van der Lee, J.: Changes in reactive surface area during limestone dissolution: an experimental and modelling study. Chem. Geol. **265**(1-2), 160–170 (2009)
79. Marty, N.C., Tournassat, C., Burmol, A., Giffaut, E., Gaucher, E.: Influence of reaction kinetics and mesh refinement on the numerical modelling of concrete/clay interactions. J. Hydrol. **364**, 58–72 (2009)
80. Prieto, M.: Thermodynamics of solid solution-aqueous solution systems. Rev. Mineral. Geochem. **70**, 47–85 (2009)